Evidence of Dislocation Mixed Climb in Quartz from the Moine and Main Central Thrusts: an Electron Tomography Study

Timmo Weidner[1], Alexandre Mussi[1], Olivier Castelnau[2], Andreas Kronenberg[3], Richard Law[4] and Patrick Cordier[1,5]

[1]Univ. Lille, CNRS, INRAE, Centrale Lille, UMR 8207 - UMET – Unité Matériaux et Transformations, F-59000 Lille, France
[2]Laboratoire PIMM, Arts et Métiers Institute of Technology, CNRS, Cnam, 151 boulevard de l'Hôpital, 75013 Paris, France
[3]Department of Geology and Geophysics, Texas A&M University, College Station, TX, USA
[4]Department of Geosciences, Virginia Tech, Blacksburg, VA 24061, USA
[5]Institut Universitaire de France, 1 rue Descartes, F-75005 Paris, France
Corresponding author: Patrick Cordier (patrick.cordier@univ-lille.fr)

Key Points:

- Deformation involves mostly <a> and <a+c> slip on pyramidal and prismatic planes; [c] glide is marginal, <a>basal is not activated
- Approximately 60% of the dislocations move by mixed climb, i.e. a combination of glide and climb
- Under natural strain-rates glide and climb velocities are comparable

Abstract

In this study we apply electron tomography to characterize 3D dislocation microstructures in two highly sheared quartz mylonite specimens from the Moine and Main Central thrusts which were deformed extensively by dislocation creep in the presence of water. Both specimens show dislocation activity with dislocation densities of the order of 3-4×10^{12} m^{-2} and evidence of recovery from the presence of subgrain boundaries. $\langle a \rangle$ slip occurs predominantly on pyramidal and prismatic planes ($\langle a \rangle$ basal glide is not active). [c] glide is not significant. On the other hand, we observe a very high level of activation of $\langle c + a \rangle$ glide in the $\{10\bar{1}0\}$, $\{10\bar{1}1\}$, $\{11\bar{2}n\}$ (n=1,2) and even $\{21\bar{3}1\}$ planes. Approximately 60% of all dislocations involve climb with a predominance of mixed climb, a deformation mechanism characterized by dislocations moving in a plane intermediate between the glide and the climb planes. This atypical mode of deformation demonstrates comparable glide and climb efficiency under natural deformation conditions. It promotes dislocation glide in planes atypical of quartz structure, probably by inhibiting lattice friction. Our quantitative characterization of the microstructure enables us to assess the strain that dislocations can generate. We show that the contribution of glide produced by the observed dislocations is sufficient to satisfy the von Mises-Taylor criterion. Hence, activation of climb is not necessary to provide additional strain components, but it contributes to the magnitudes of strains achieved. On the basis of this characterization, we propose a numerical modelling approach for attempting to characterize the local stress state that gave rise to the observed microstructure.

Plain Language Summary

In this study, we propose advanced transmission electron microscopy characterization of microstructures generated in quartz deformed in natural shear zones to better understand the geological deformation conditions and the response of quartz to applied stresses during deformation. We characterize the crystal defects responsible for the deformation of the mineral. We highlight an original deformation mechanism activated at very low natural strain rates only.

1 Introduction

Quartz is one of the major constituents, by volume, of the Earth's crust. Above *ca.* 300 °C (corresponding to depths beyond 10 km, Stipp et al., 2002a), quartz is ductile and it appears to be one of the weaker minerals in naturally deformed rocks of the continental crust. The plasticity of quartz is thus important to the description of the rheology of the lower crust. Many studies over the last 60 years have been devoted to the plasticity of quartz. Still, the plastic behaviour of this mineral is only partially understood, even in the laboratory. Our understanding of the plasticity of this mineral under natural conditions and its control of crustal rheology is far from resolved. The simple question of crystal plasticity of quartz by glide of dislocations is not straightforward. In this trigonal mineral, glide of <a> dislocations ($1/3\ \langle 2\bar{1}\bar{1}0 \rangle$) in the basal plane is expected (Baëta & Ashbee, 1969). It was indeed observed

experimentally very early on and is complemented at higher temperatures by glide of [c] ([0001]) dislocations in prismatic planes (Blacic, 1975). However, these slip systems by themselves are insufficient to satisfy the von Mises-Taylor criterion for general strains with arbitrary non-zero components (von Mises 1928; Taylor 1938, Ball & White 1978). Activating <c+a> glide can potentially satisfy the remaining strain components (Baëta & Ashbee 1969, Trépied & Doukhan, 1982): however, this mechanism seems to have been neglected for several years. Also, dislocation glide is not the only possible deformation mechanism in quartz. Additional degrees of freedom to deformation may be facilitated by dislocation climb as point defects become mobile through diffusion. Strains may also be satisfied by sliding at grain boundaries (Behrmann & Mainprice 1987; Fliervoet et al. 1997; Rutter & Brodie 2004, Fukuda et al. 2018 and Tokle et al. 2019).

Beyond the fundamental questions about intracrystalline deformation mechanisms that apply to all minerals (and crystalline solids in general), dislocation creep of quartz and its mechanical properties depend on impurities, particularly those derived from water (such as hydroxyls at structural sites of the crystalline structure and dislocations). Owing to the three-dimensional network of strong Si-O bonds, dry quartz is very strong, and almost undeformable by dislocation motions in the laboratory. In contrast, quartz deformed at tectonic strain rates in the presence of water (at temperatures greater than 400 °C) is ductile and appears to be one of the weakest minerals of quartzo-feldspathic crustal rocks.

The phenomenon of water (or hydrolytic) weakening was discovered by Griggs and Blacic (1965) and interpreted to result from hydrolysis of strong Si-O-Si bonds, to form weak hydrogen-bonded SiOH groups at dislocation cores (Griggs, 1967, 1974). Hydrous defects were originally thought to be transported to dislocation cores by volume diffusion. However, alternative water weakening models have since been proposed, including potential effects of hydrogen impurities on other, charged point defects that facilitate climb (Hobbs, 1981, 1984), and effects of hydrogen impurities on concentrations (and mobilities) of dislocation kinks and jogs (Hirsch, 1981). All of these models have been challenged, though, by the discovery that solubilities of OH defects within the quartz structure are low (Doukhan & Paterson, 1986; Kronenberg et al., 1986; Cordier & Doukhan, 1989, 1991), limiting the predicted changes in point defect chemistry of crystalline quartz and the delivery of OH to dislocations cores by radial volume diffusion to dislocation cores. *Ab initio* models of hydrous molecular structures and dislocation kinks in quartz indicate that hydrous defects are stable at dislocation cores, particularly at dislocation kinks (Heggie et al., 1985; Heggie & Jones, 1986). Hydrous defects are therefore thought to gain access to dislocation cores by pipe diffusion from grain

boundaries or fluid inclusions (Cordier et al., 1988; Cordier & Doukhan, 1989, 1991; Bakker & Jansen, 1990, 1994; Heggie, 1992).

Hydrolytic weakening has only been observed when measured OH concentrations are supersaturated with respect to hydrous defect solubilities (Kekulawala et al., 1978, 1981; Kirby & McCormick, 1979; Cordier & Doukhan, 1989). Initial transient creep rates of OH-supersaturated quartz have been explained by mechanisms of dislocation nucleation at non-equilibrium water clusters and fluid inclusions with further dislocation multiplication facilitated by pipe diffusion of hydrous defects (Cordier & Doukhan, 1989; Gerretsen et al., 1989: McLaren et al., 1989). Most relevant to the present study is the role of hydrous defects in facilitating dislocation climb during plastic deformation of quartz.

Dislocation climb is usually regarded as a recovery mechanism rather than a strain-producing mechanism (Tullis & Yund 1989). However, activation of the climb mechanism proposed by Nabarro (1967) was suggested by Ball & White (1978) and Ball & Glover (1979) to apply to quartz single crystals experimentally compressed along the [0001] direction. The activity of dislocation climb in quartz also has implications for the onset of dynamic recrystallization (Hirth & Tullis 1992). In the absence of significant contributions from dislocation climb at low temperature, recovery can occur by strain-induced grain boundary bulging recrystallization. At higher temperature, when dislocation climb is enhanced, recrystallization may occur by progressive subgrain rotation (Hirth & Tullis 1992).

In a recent study, we applied an analytical method to quartz using electron tomography of dislocation microstructures to determine the components of the plastic strain tensor (Mussi et al. 2021b) resulting from the displacement of these dislocations. This study revealed the unexpected activation of <c+a> dislocation climb. The present study was undertaken to learn whether <c+a> dislocation climb is important to the plastic deformation of quartz in natural shear zones, and learn whether this process may be linked to water weakening. Quartz mylonite specimens were selected for electron tomography from the Moine and Main Central thrusts, both of which deformed extensively by dislocation creep in the presence of water. Abundant fluid inclusions that intersect with dislocations suggest that dislocation mobilities in these specimens may have been facilitated by access to hydrous defects within dislocation cores that increase rates of dislocation glide and/or climb. TEM tomography of dislocations presented in this study is applied to determine the relative mobilities of dislocations by glide and climb.

2 Materials and Methods

132 2.1 Specimens

133 Two highly sheared quartz mylonite specimens have been chosen for this study, which exhibit
134 optical microstructures and crystallographic preferred orientations due to dislocation creep
135 and dynamic recrystallization. Both mylonites come from major shear zones of collisional
136 tectonic boundaries, one from the gently SE-dipping Moine Thrust of Northwest Scotland,
137 associated with Caledonian shortening of the foreland continental margin during closure of
138 the Iapetus Ocean (Strachan et al., 2002; Law et al., in press), and the other from the Main
139 Central Thrust of Northwest India, associated with southward-directed Oligocene-Miocene
140 extrusion of the Greater Himalayan slab (Hodges, 2000). The Moine Thrust mylonite
141 specimen SG-10 (hereafter referred to as MT) was collected from Cambrian quartzites of the
142 footwall exposed at the Stack of Glencoul, just 4.6 m below the thrust contact with overlying
143 Neoproterozoic Moine schists (Law et al., 1986, 2010). The Main Central Thrust mylonite
144 specimen S-09-35a (hereafter referred to as MCT) was collected from a quartz-rich horizon of
145 Greater Himalayan orthogneisses exposed in the western part of the Sutlej Valley, at a
146 structural distance of 71 meters above the Main Central Thrust (Law et al., 2013).
147 Moine thrust specimen SG-10 (MT) consists of sheared ribbon quartz grains with smooth
148 undulatory extinction observed in conventional thin sections, and well-developed subgrain
149 walls that are apparent in ultra-thin sections (~5 μm) (Kronenberg et al., 2020), consistent
150 with optical microscopy of etched sections and transmission electron microscopy (TEM) of
151 nearby mylonitic Cambrian quartzites (Ord & Christie, 1984). Ribbon quartz grains are
152 recrystallized at their margins, with microstructures due to grain boundary bulging (BLG) and
153 subordinate subgrain rotation (SGR) (Stipp et al., 2002b; Law, 2014); over 70 % of this
154 specimen consists of recrystallized grains (with a 21 μm mean size; Weathers et al., 1979;
155 Kronenberg et al., 2020) but the new TEM observations of this study are from original ribbon
156 quartz grains. Crystallographic c-axes of ribbon and recrystallized quartz grains exhibit nearly
157 symmetric crossed-girdle patterns aligned with respect to grain shape foliation and lineation
158 (Law et al., 2010), consistent with significant plane-strain foliation-normal shortening by
159 glide on multiple slip systems with Burgers vectors parallel to *a* and to *c* (and other
160 crystallographic slip vectors with components in *a* and *c*).
161 The temperature of deformation for the leading edge of the Moine thrust, based on
162 crystallinity of white micas, is relatively low, 300-350 °C (Johnson et al., 1985), while
163 temperature estimates for SG-10 based on opening angles of quartz c-axis fabrics measured
164 on ribbon detrital quartz grains (53°) and matrix recrystallized quartz grains (69°) are as large
165 as 415 °C and 525 °C respectively (Law et al., 2010; Faleiros et al. 2016 opening angle

thermometer). Peak lithostatic pressures during mylonitization have not been determined. The differential stress estimated from the mean recrystallized grain size (21 μm) of SG-10 and the modified Stipp et al. (2006) recrystallized grain size piezometer (with the adjustment of Holyoke & Kronenberg, 2010) is ~44 MPa, and strain rates based on this stress, temperature estimates of 350 – 400 °C, and the quartzite flow law of Hirth et al. (2001) are between 10^{-14} s^{-1} and 10^{-13} s^{-1}.

Infrared absorption measurements of OH bands of original ribbon quartz grains of SG-10 are large, varying from one grain to another, with molar OH/Si concentrations of 2400 ($\pm$700) ppm (H/10^6 Si) (Kronenberg et al., 2020). Preliminary TEM observations corroborate earlier observations of intimate dislocation-fluid inclusion relationships (Ord & Christie, 1984), which indicate that intragranular water contents were large at the time of deformation and that hydrogen defects had direct access to dislocations.

Main Central Thrust specimen S-09-35a (MCT) is made up of highly sheared quartz horizons within a sheared matrix of mixed quartz and layer silicates. Almost all quartz horizons of this specimen have been recrystallized, but the TEM observations made here are for larger residual quartz grains whose deformation gives them the grain shapes of augen. These quartz augen exhibit patchy undulatory extinction and well-developed subgrain walls. Fine recrystallized quartz grains appear within the larger grains and at their margins, with microstructures that indicate that recrystallization occurred predominantly by subgrain rotation (SGR) with subordinate grain boundary migration (GBM) (Stipp et al., 2002; Law et al., 2013). The mean recrystallized grain size measured in quartz-rich layers is ~ 45 μm (Francsis, 2012), suggesting lower differential stresses during deformation of this specimen compared with SG-10 from the Moine thrust zone. Crystallographic c-axes of recrystallized quartz-rich horizons show distinctly asymmetric cross-girdle patterns, with high c-axis densities defining a great circle consistent with oblique grain shape alignments subparallel to lineation and top-to-the SW (thrust) shear (Law et al., 2013).

Using the Faleiros et al. (2016) opening angle thermometer, the temperature of deformation for S-09-32a is estimated to be 515 °C, based on a measured c-axis fabric opening angle of 68° (Law et al., 2013). In contrast to the differences in crystal fabric and petrologically based temperatures of Moine thrust specimens at the Stack of Glencoul, estimates of peak deformation and metamorphic temperatures, based on c-axis patterns and coexisting garnet and muscovite compositions of mylonites collected from the Sutlej Valley, are in close agreement. Peak pressures estimated for mylonites ~1100 m structurally above S-09-35a are of the order of 800 MPa (Supplementary file in Law et al. 2013). The differential stress

estimated from the mean recrystallized grain size of S-09-35a and the modified Stipp et al. (2006) piezometer is ~ 24 MPa (Francsis 2012, Law et al. 2013). The strain rate predicted by the Hirth et al. (2001) flow law at these conditions is ~10^{-12} s^{-1}.

Infrared absorption measurements of OH bands reveal large but variable OH contents of large augen quartz grains with mean molar OH contents of 3010 ($\pm$ 2780) ppm (Kronenberg et al., 2017). These bands are due to intragranular molecular water, and preliminary TEM shows that fine fluid inclusions routinely decorate dislocations. To the best of our knowledge, no previous TEM-based studies have been carried out on high strain rocks located adjacent to the MCT and exposed in the Sutlej Valley

While the inferred temperatures, pressures, differential stresses and strain rates of the two mylonite specimens investigated in this study vary, the overall crystallographic fabrics are remarkably similar. With their similar quartz cross-girdle c-axis fabrics and fabric opening angles for the MT and MCT specimens (53° and 69° measured for deformed detrital and recrystallized grains, respectively, in SG-10, and 68° for recrystallized grains in S-09-32a), we might expect similar dislocation slip systems to be important with similar proportions of slip vector components in the a and c directions.

Temperature estimates for these specimens correspond well with the temperature ranges for dynamic recrystallization of quartz by BLG, SGR, and GBM mechanisms (Stipp et al., 2002); subgrain rotation recrystallization appears to be important for both mylonites, with the implication that dislocation climb is important in both tectonic settings and deformation conditions. In addition to SGR recrystallization, the MT specimen exhibits evidence for BLG recrystallization, while the MCT specimen has grain boundaries characteristic of some GBM recrystallization.

2.2 Transmission electron microscopy

Dislocation Electron Tomography (DET) reconstructs in 3D the dislocation microstructure (Barnard et al. 2006). This method differs from that of conventional tomography studies, since DET is based on diffraction contrast. Dislocations in the specimens from the Main Central Thrust (MCT) and the Moine Thrust (MT) zone are imaged using the high-structure factor $11\bar{2}2$ and $1\bar{1}01$ diffraction vectors, respectively. DET requires precise alignment of the diffraction vectors along the tilt axis (with an accuracy of $\pm$ 0.1°) in order to maintain constant diffraction contrast conditions for images acquired over the entire tilt series. Once this key alignment is satisfied, a tilt-series of images is acquired, capturing several micrographs of the region of interest for numerous tilt angles (generally consisting of approximately 60 projected images acquired over every two degrees of tilt). DET analyses were carried out using the

electron microscopy facility of the Advanced Characterization Platform of the Chevreul Institute, with a FEI® Tecnai $G^2$20Twin microscope, operating at 200 kV equipped with a LaB_6 filament. TEM analyses were conducted with a high-angle triple-axis sample-holder (Hata et al., 2011) with a maximal angular range of ± 80° in Weak-Beam Dark-Field (WBDF) and with a conventional double-tilt sample-holder with a maximal angular range of ± 60° in Weak-Beam Bright-Field (WBBF) conditions. As quartz is known to be electron beam sensitive, special precautions were taken during acquisition:

- TEM analyses were performed with a small condenser aperture of 100 µm in diameter and a small spot size of 11.3 nm in diameter.
- To highly enhance the WBDF micrographs signal-to-noise ratio, without increasing the electron dose, pixels have been gathered four by four.
- Last but not least, tilt-series were acquired with fewer projected images than normally employed in DET (less than 30 micrographs), before much damage was observed.

For the MCT specimen, WBDF micrographs were acquired every 5° from -55° to 70° (tilt-series composed of 26 projected images), and for the MT specimen, WBBF micrographs were acquired every 10° from -50° to 50° and for -45° to 35° (tilt-series composed of 11 and 9 projected images respectively). Relations between the crystal reference system and the specimen reference system were obtained simulating electron diffraction patterns with the 'Electron Diffraction' software from Morniroli (1994). Since dislocation contrast is intrinsically weak in WBDF mode, the tilt-series alignment must be conducted manually with one-pixel accuracy employing Gatan® image alignment software. Each WBDF micrograph was numerically filtered with the background subtraction option of ImageJ software, to enhance the dislocation contrast of the tilt-series obtained with an intermediate number of projected images (26 micrographs). Given that the tilt-series for quartz was obtained with relatively few projected images (9 and 11 WBBF micrographs), each dislocation of each micrograph was redrawn to consider only the position of the dislocation line (following the analytical method of Mussi et al., 2021b). Image reconstruction was conducted using the Weighted Back Projection (WBP) algorithm (Herman et al., 1976), based on the Radon transformation (Radon, 1983). The WBP algorithm is freely available with the TomoJ plugin (Messaoudi et al., 2007) accessible in ImageJ. This reconstruction generates a volume which is interpolated in the angular range of acquisition and extrapolated in the missing-wedge. This method leads to ribbon shapes of the reconstructed dislocations (thin dislocation widths in the acquisition angular range and thick dislocation widths in the missing-wedge). The UCSF Chimera free software (Pettersen et al., 2004) is used to redraw the dislocations in the volume

which re-establishes the cylindrical geometries of the dislocations (Liu et al., 2011; Mussi et al., 2016).

2.3 Burgers vector indexation method

Burgers vector identifications were conducted using the invisibility criterion $\mathbf{g} \cdot \mathbf{b} = 0$, where $\mathbf{g}$ is the considered diffraction vector and $\mathbf{b}$ is the Burgers vector. Dislocation intensity has also been used for indexing, knowing that the peak value of the dislocation intensity in weak-beam conditions is assumed to be approximately proportional to $(\mathbf{g} \cdot \mathbf{b})^2$ (De Ridder & Amelinckx, 1971). The thickness fringe method developed by Ishida et al. (1980) was also used to index Burgers vectors in order to reduce the necessary number of micrographs required for our analyses. This technique consists of counting the number of thickness fringes observed for dislocations that intersect thin foil surfaces (this number corresponds to the $|\mathbf{g} \cdot \mathbf{b}|$ product). Consequently, just three independent diffraction conditions were sufficient for Burgers vector characterization.

2.4 Potential plastic strain associated with dislocation segments

Most of the dislocation segments observed in this study lie out of their glide plane. This configuration is discussed in section 4.3. These dislocation segments must be analysed, recognizing that they must have moved by a combination of glide and climb. In the following, we express the strain that can be generated by the displacement of the dislocation segments present in the specimen, taking into account their movement plane. The geometry is represented schematically in Figure 1. We denote $\mathbf{n}$ the unit vector normal to the plane containing the dislocation line (referred to as the movement plane), and $\mathbf{n}^{\mathrm{g}}$ the unit vector normal to the glide plane (index $.^{g}$ stands for 'glide'). The Burgers vector $\mathbf{b}$ is thus perpendicular to $\mathbf{n}^{\mathrm{g}}$ (Figure 1). The unit line vector of the dislocation, denoted $\mathbf{l}$, is in the movement plane and is therefore perpendicular to $\mathbf{n}$. For the part of a segment that is edge oriented, the line vector, denoted $\mathbf{l}^{e}$ (index $.^{e}$ stands for 'edge') is also perpendicular to the Burgers vector. Therefore, it can be expressed as

$$\mathbf{l}^{e} = \frac{\mathbf{b} \times \mathbf{n}}{\|\mathbf{b} \times \mathbf{n}\|} \quad (1)$$

where '×' is the cross product. The normal $\mathbf{n}^{g}$ of the dislocation glide plane is perpendicular to both the line vector $\mathbf{l}^{e}$ and the Burgers vector $\mathbf{b}$ and can thus be written

$$\mathbf{n}^{g} = \frac{\mathbf{l}^{e} \times \mathbf{b}}{\|\mathbf{l}^{e} \times \mathbf{b}\|}. \quad (2)$$

The dislocation (edge or screw) gliding in that plane produces a plastic strain-rate proportional to its Schmid tensor $\mathbf{S}^{g}$, according to the Orowan equation

$$\dot{\varepsilon}_{ij}^{g} = \rho b v^{g} S_{ij}^{g} \quad (3)$$

with $S_{ij}^{g} = \frac{1}{2}\left(n_i^g \hat{b}_j + n_j^g \hat{b}_i\right)$, where $\hat{\mathbf{b}}$ is the unit vector parallel to **b**, ρ is the density of mobile dislocations and v^g is their glide velocity. The inclination θ between the dislocation plane and the glide plane (Figure 1) can be calculated from $\cos\theta = \mathbf{n}^g.\mathbf{n}$. For non-zero values of θ, climb must be involved. The kinematics of the climb of an edge dislocation is a little more complicated as diffusion may not produce an isochoric strain (see Lebensohn et al., 2010 and Yuan et al., 2018). However, considering geological time scales, we assume that the density of point defects that affect climb achieves equilibrium concentrations (*i.e.* constant with time) at a given temperature. Thus, no volume change is expected due to climb. The strain-rate tensor produced by climb is proportional to the 'climb Schmid tensor' $\mathbf{S}^c$ (index $.^c$ stands for climb)

$$\dot{\varepsilon}_{ij}^{c} = \rho b v^c S_{ij}^{c} \tag{4}$$

where v^c is the climb rate of the segment and $\mathbf{S}^c$ is given by $S_{ij}^{c} = \hat{b}_i\hat{b}_j - \frac{1}{3}\hat{b}_k\hat{b}_k\delta_{ij}$. As indicated in Tables SI and SII (in supplementary materials), several dislocation segments and movement planes have been identified in the two grains investigated. Grain deformation can be investigated by summing-up the contributions of glide and/or climb of one or more dislocation segments, and the number of the associated independent deformation systems can be computed as explained in Castelnau et al. (2020) for any crystal symmetry.

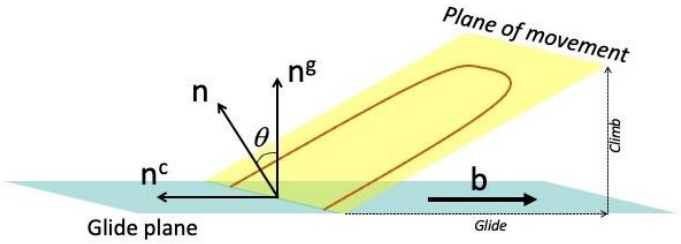

Figure 1: Geometry of a dislocation in mixed climb configuration i.e. where the plane of movement (identified by its normal **n**) is intermediate between the glide plane and the climb plane. $\mathbf{n}^g$ is the normal of the dislocation glide plane, $\mathbf{n}^c$ is the normal of the dislocation climb plane. **b** is the Burgers vector.

2.5 Estimation of the local loading conditions

Here we attempt to infer the local stress that acted *in situ* on the investigated grain to produce the observed dislocation microstructure. We assume a power law constitutive relation for glide and for climb to estimate the dislocation velocity for glide and climb. These velocities, which depend on the local stress, are linked together by the angle θ shown in Figure 1.

329 2.5.1 Glide

330 We start with the Orowan equation (Eq. 3), written for a specific slip system and consider a
331 standard power-law (Morales et al. 2011) to describe the shear-rate at the slip system scale:

332 $$\dot{\gamma} = \dot{\gamma}_0 \left|\frac{\tau}{\tau_0}\right|^{n_g-1} \frac{\tau}{\tau_0} \quad (5)$$

333 where $\dot{\gamma}_0$ is a reference strain-rate, τ_0 is the corresponding reference stress, n_g gives the stress
334 sensitivity for glide, and τ is the shear stress resolved on the glide plane given by:

335 $$\tau = n_i^g \hat{b}_j \sigma'_{ij} \quad (6)$$

336 The dislocation glide velocity is thus given by:

337 $$v_g = \frac{\dot{\gamma}_0}{\rho b} \left|\frac{\tau}{\tau_0}\right|^{n_g-1} \frac{\tau}{\tau_0} \quad (7)$$

338 *2.5.2 Climb*

339 Here we use the Orowan equation (Eq. 4) adapted to climb, following Lebensohn et al.
340 (2010). As for glide, we consider a standard power-law to describe the longitudinal strain-
341 rate:

342 $$\dot{\varepsilon} = \dot{\gamma}_0 \left|\frac{\sigma'}{\sigma_0}\right|^{n_c-1} \frac{\sigma'}{\sigma_0} \quad (8)$$

343 where $\dot{\gamma}_0$ is a reference strain-rate (which can be taken as the same as for glide), σ_0 is the
344 corresponding reference stress, n_c gives the stress sensitivity for climb, and σ' is the
345 deviatoric stress given by:

346 $$\sigma' = \hat{b}_l \hat{b}_j \sigma'_{ij} \quad (10)$$

347 The dislocation climb velocity is thus given by:

348 $$v_c = \frac{\dot{\gamma}_0}{\rho b} \left|\frac{\sigma'}{\sigma_0}\right|^{n_c-1} \frac{\sigma'}{\sigma_0}. \quad (11)$$

349 *2.5.3 Estimation of the local stress*

350 The velocities v_c and v_g are related by the angle θ between the normal to the plane of
351 movement and the normal to the glide plane. This can be expressed as

352 $$\left(v_g \hat{\mathbf{b}} + v_c \mathbf{n}^g\right).\mathbf{n} = 0 \quad (12)$$

353 where $\cos\theta = \mathbf{n}^g.\mathbf{n}$. To find a stress state compatible with the observed dislocation structure,
354 we must solve for a system of nonlinear equations formed by one condition (12) for each
355 observed dislocation segment. We adopt a minimization procedure in order to find the stress
356 tensor that best matches the observations. We construct the following objective function

357 $$\sum_s \; l_s^k (\theta_s^{mod} - \theta_s^{obs})^2 \quad (13)$$

358 where θ^{mod} is the θ angle computed from the above equations and θ^{obs} is the observed
359 angle. The difference in θ angles is weighted by the dislocation length *l* to the power *k* in

order to force a better match for longer dislocation segments (here, we used a value for $k = 4$). The objective function is the sum over all observed dislocation segments s, minimized by the Nelder-Mead method.

3 Results

The dislocation microstructures of the MCT and MT specimens are comparable. Dislocation densities are 3×10^{12} m^{-2} and 4×10^{12} m^{-2} respectively (with densities measured directly from the reconstructed volumes). Sub-grain boundaries due to recovery are observed in both specimens (Figures 2 and 3).

In this section, the quantitative analysis of the microstructure is described, followed by a detailed characterization of slip systems, and then climb systems for each specimen. From these analyses, Schmid tensors and associated equivalent strain and stress tensors of each specimen are estimated.

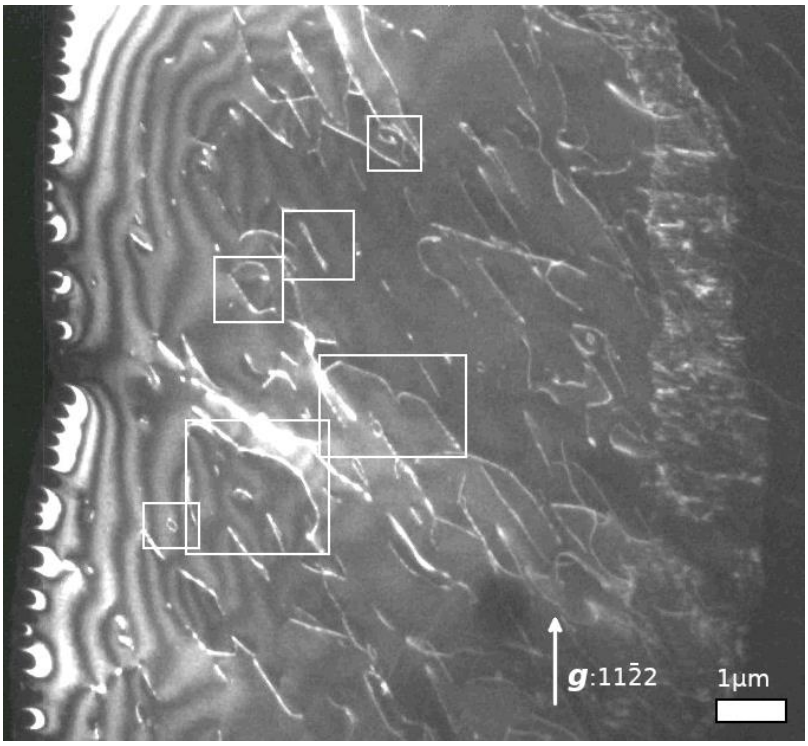

Figure 2: Global microstructure of the specimen from the MCT: Micrograph in WBDF condition obtained with the $11\bar{2}2$ diffraction vector (the white rectangles are analysed in detail in this study), where one sub-grain can be observed.

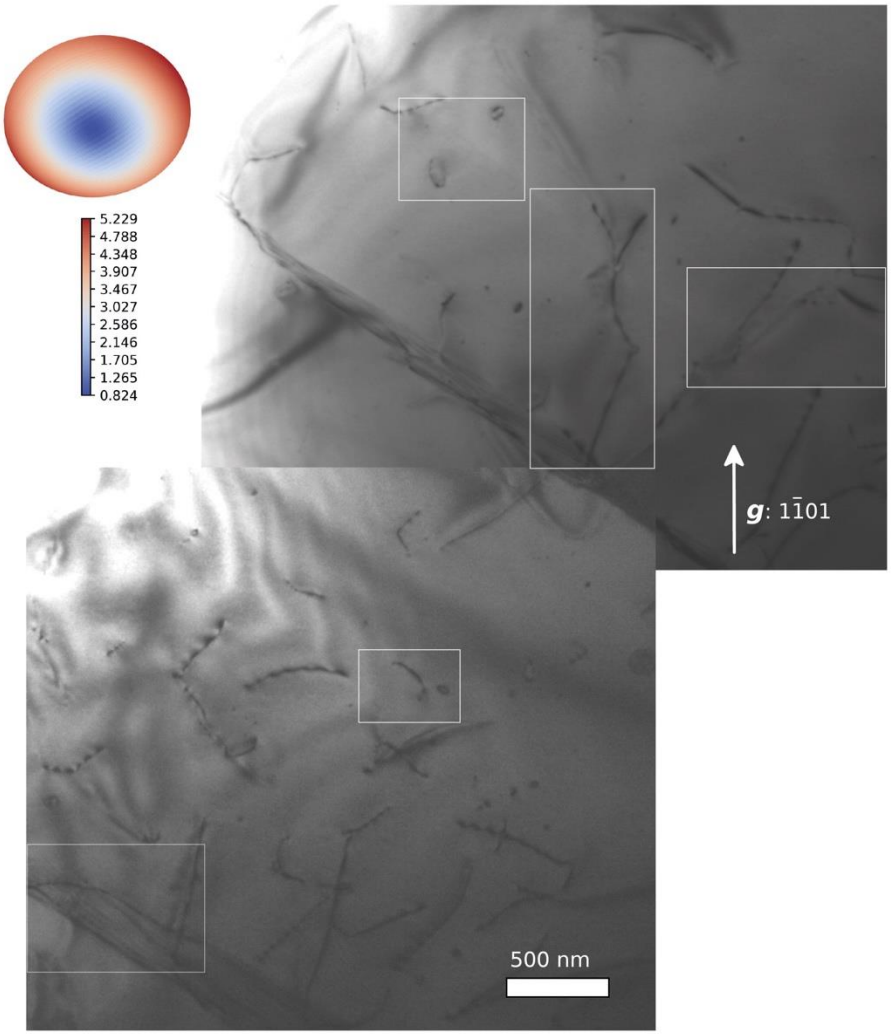

Figure 3: Global microstructure of specimen from the MT: Micrograph in WBBF condition obtained with the $1\bar{1}01$ diffraction vector (the white rectangles are analyzed in detail in this study) where two sub-grains can be observed. In the top left corner is the stress ellipsoid inferred from the present analysis (see discussion, Figure 12 and Supplementary movie).

3.1 Quantitative analysis of the microstructure

The characterization of dislocation glide and/or climb relies on determination of the plane of movement of the dislocation, which can only be achieved for curved dislocations. In this study, however, we have sought to take into account the contribution of rectilinear dislocations to the microstructure. Lattice friction is high in quartz under the deformation conditions of our specimens (Doukhan & Trépied, 1985). Consequently, it is highly likely that rectilinear dislocations are in glide configurations. Following the characterization of direction lines of rectilinear dislocations with known Burgers vectors, it is possible to infer their glide planes (provided that they are not pure screw in character). In order to optimize the quantification of the dislocation glide and climb contributions, we have only considered the

dislocations whose Burgers vectors could be determined unambiguously, keeping in mind that indexing of Burgers vectors has previously been optimized (see section *2.3*). However, DET has been conducted for each specimen with only one diffraction vector which does not allow identification of all dislocation segments. More precisely, the DET study of the MCT specimen has been conducted with the $11\bar{2}2$ diffraction vector, where all dislocations ($\langle a \rangle$, [c] and $\langle c+a \rangle$) are in contrast except $\boldsymbol{c+a_3}$ dislocations. Our DET study of the MT specimen has been conducted with the $1\bar{1}01$ diffraction vector where all dislocations are in contrast except $\boldsymbol{a_3}$, $\boldsymbol{c+a_2}$ and $\boldsymbol{c-a_1}$.

3.2 Glide

3.2.1 MCT specimen

In this specimen, we found evidence of $\langle a \rangle$ and $\langle c+a \rangle$ glide in prismatic $\{1\bar{1}00\}$ planes, and also of $\langle a \rangle$ glide in pyramidal $\{1\bar{1}01\}$ planes and in a $(1\bar{1}02)$ pyramidal plane.

An example of tomographic reconstruction of a typical domain is shown in Figure 4. The Burgers vector indexing shows the presence of dislocations with $\frac{1}{3}[1\bar{2}10]$ (or $\boldsymbol{a_2}$) and $\frac{1}{3}[1\bar{2}13]$ (or $\boldsymbol{c-a_2}$) Burgers vectors, drawn in light and dark green, respectively. The reconstructed dislocation volumes can be tilted to view the planes containing these dislocations edge-on. Figures 4a-c, show an $\boldsymbol{a_2}$ dislocation lying near the prismatic $(10\bar{1}0)$ plane. This demonstrates activation of the $\frac{1}{3}[1\bar{2}10](10\bar{1}0)$ slip system. A slightly more complex configuration is detailed in Figures 4d-f. Part of this dislocation is in the $(10\bar{1}0)$ glide plane. Moreover, a collinear interaction (Madec et al., 2003; Mussi et al., 2015) with an $\boldsymbol{a_2}$ sessile dislocation loop can be clearly identified. The plane of this loop is edge-on for a projection angle[1] of -38° (Figure 4f). The 3D geometry of this dislocation is due to this interaction. From Figures 4g-i, we also characterize the $\frac{1}{3}[1\bar{2}13](10\bar{1}0)$ slip system.

[1] A projection angle is the angle between the normal of the specimen thin foil and the direction of the electron beam for a particular tilt angle.

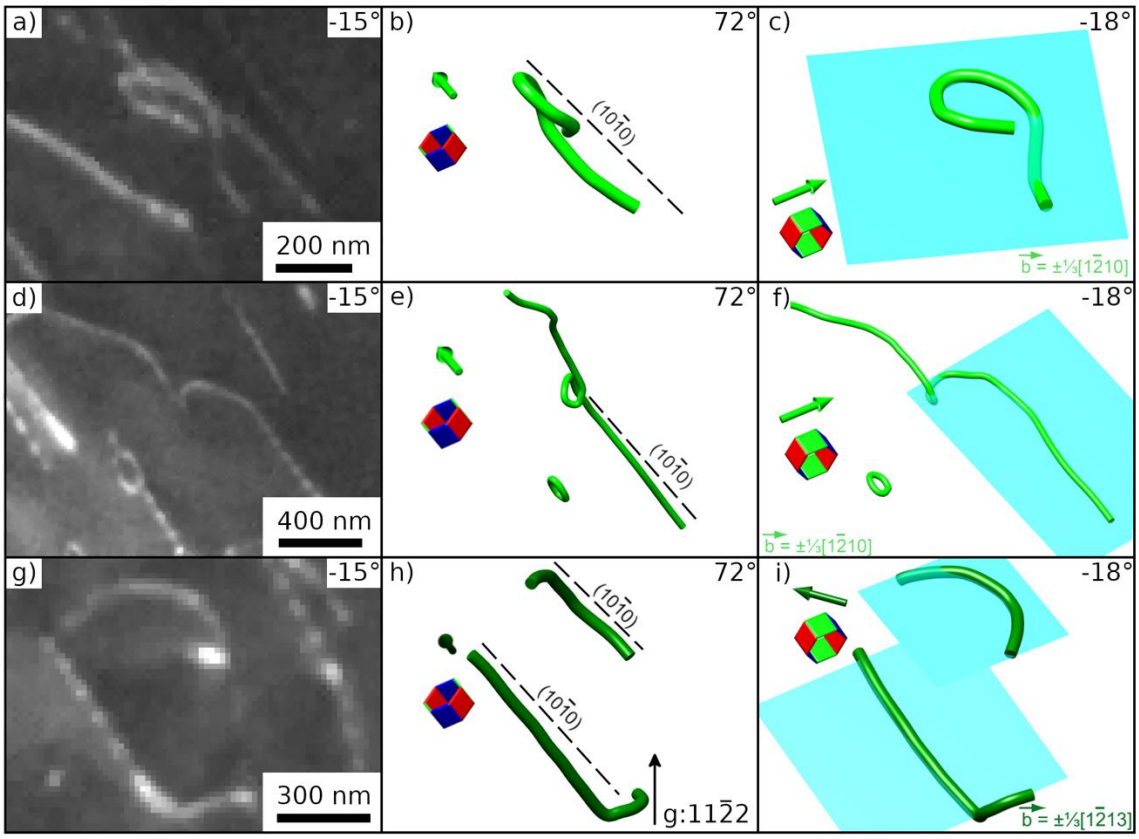

Figure 4: Slip system characterizations by dislocation electron tomography for the MCT specimen, obtained with the $11\bar{2}2$ diffraction vector: a) Raw WBDF micrograph of a $\boldsymbol{a_2}$ dislocation observed along a projection angle of -15°; b) reconstructed volume of this dislocation (coloured in green) for a projection angle of 72° where the prismatic $(10\bar{1}0)$ plane is edge-on; c) same reconstructed dislocation with a projected angle of -59°; d) raw WBDF micrograph of two $\boldsymbol{a_2}$ dislocations (a dislocation loop and a complex 3D dislocation) observed along a projection angle of -15°; e) reconstructed volume of these dislocations for a projection angle of 72°; f) same reconstructed dislocations with a projected angle of -38°; g) raw WBDF micrograph of 3D $\boldsymbol{c-a_2}$ dislocations observed along a projection angle of -15°; h) reconstructed volume of these dislocations (coloured in dark green) for a projection angle of 72°; i) same reconstructed dislocations with a projected angle of -29°. The $\frac{1}{3}[\bar{1}2\bar{1}0](10\bar{1}0)$ and $\frac{1}{3}[1\bar{2}13](10\bar{1}0)$ slip systems have been characterized in this figure. (For interpretation of the references to colour in this caption, the reader is referred to the web version of this article)

3.2.2 MT specimen

The MT specimen also shows dislocations in glide configurations. We found evidence for glide of $\langle a\rangle$, [c] and $\langle c+a\rangle$ dislocations. In this specimen, no prismatic glide has been observed for $\langle a\rangle$ and $\langle c+a\rangle$ dislocations; only [c] dislocations in $(1\bar{1}00)$ and $(\bar{2}110)$ glide planes have been characterized. $\langle a\rangle$ dislocations appear to glide predominantly in $\{1\bar{1}01\}$ pyramidal planes. We have also noted evidence for $\langle a\rangle$ glide in $\{1\bar{1}02\}$ and $\{2\bar{2}01\}$, and $\langle c+a\rangle$ glide in $\{\bar{1}01\bar{1}\}$, $\{11\bar{2}\bar{1}\}$, $\{11\bar{2}2\}$ and $\{21\bar{3}\bar{1}\}$. Glide in $\{1\bar{1}01\}$ represents approximately 3/7 of all dislocation glide evaluated in this specimen. An example of a slip

system characterization is shown in Figures 5a-d. The pyramidal $(11\bar{2}\bar{1})$ plane is edge-on with a projection angle of 14°. The direction of the trace of this plane corresponds to the direction of the dislocation line with a projection that is rectilinear, as its movement plane is edge-on (Figure 5b). The $\frac{1}{3}[2\bar{1}\bar{1}3](11\bar{2}\bar{1})$ slip system has been identified given that the Burgers vector of this dislocation is $\boldsymbol{c}+\boldsymbol{a_1}$. We have also identified the $[0001](2\bar{1}\bar{1}0)$ slip system (Figures 5e-h).

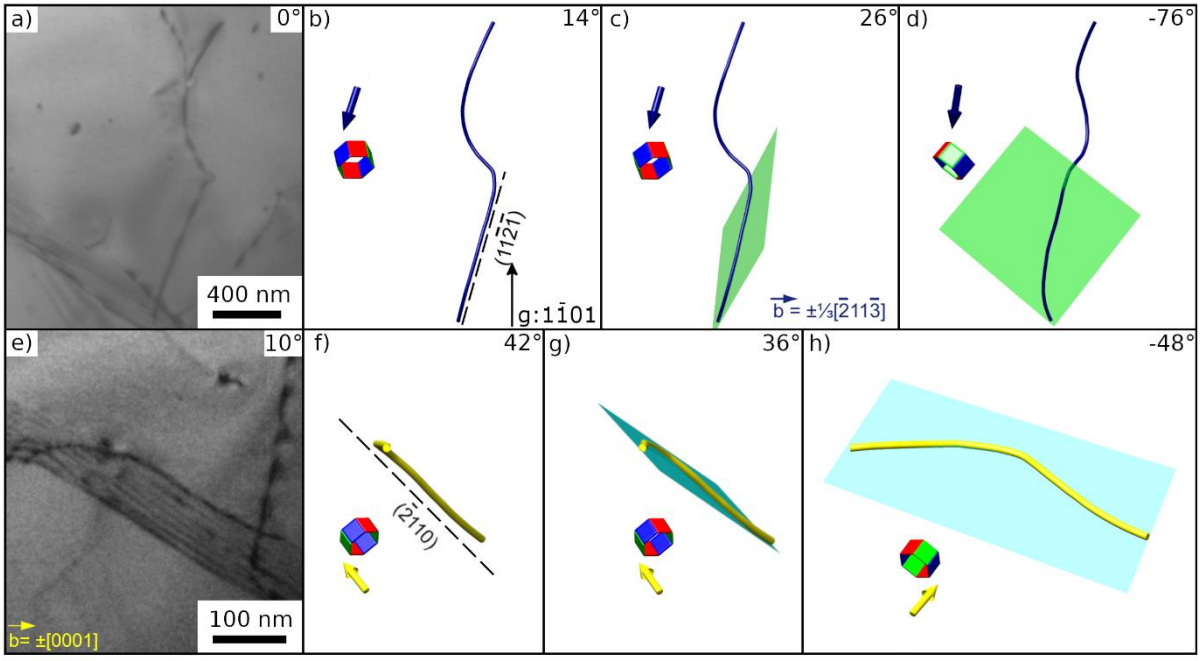

Figure 5: Slip system characterizations revealed by dislocation electron tomography, obtained with the $1\bar{1}01$ diffraction vector, in the MT specimen: a) Raw WBDF micrograph of a $\boldsymbol{c}+\boldsymbol{a_1}$ dislocation observed along a projection angle of 0°; b) reconstructed volume of this dislocation (coloured in dark blue) for a projection angle of 14° where the pyramidal $(11\bar{2}\bar{1})$ plane is nearly edge-on; c) same reconstructed dislocation with a projected angle of 26° (green plane shows the habit plane of the dislocation segment); d) same reconstruction with a projected angle of -76° (the normal to the pyramidal plane is edge-on); e) raw WBDF micrograph of a [c] dislocation observed along a projection angle of 10°; f) reconstructed volume of this dislocation (coloured in yellow) for a projection angle of 42° where the prismatic $(\bar{2}110)$ plane is edge-on; g) same reconstructed dislocations with a projected angle of 36°; h) same reconstruction with a projected angle of -48° (the normal to the prismatic plane is edge-on). The $\frac{1}{3}[\bar{2}11\bar{3}](11\bar{2}\bar{1})$ and $[0001](\bar{2}110)$ slip systems have been characterized in this Figure. (For interpretation of the references to colour in this caption, the reader is referred to the web version of this article)

3.3 Climb

3.3.1 MCT specimen

A significant proportion of the dislocation population cannot be interpreted as resulting from glide (*i.e.* lying in a plane which contains the Burgers vector). For instance, Figures 6a-c show a $\frac{1}{3}[11\bar{2}0]$ dislocation ($\boldsymbol{a_3}$) in a $(11\bar{2}0)$ plane. This corresponds to a prismatic loop in pure climb configuration. A complex 3D dislocation (Figure 6d-f) has been analysed where one of its segments is practically in pure climb configuration (Figure 6f) and three other segments are neither in pure climb, nor in pure glide configurations. In other words, the Burgers vector of this dislocation makes an angle with the plane containing each segment under consideration with values between 0 and 90° (such as in Figure 1). These configurations are characterized as mixed climb, as kinematically described in section 2.4. We also note that this dislocation shows collinear climb interaction with a prismatic loop. Figures 6g-i show an example of mixed climb, which involves a $\boldsymbol{c - a_2}$ dislocation. Of all dislocations analyzed in the MCT specimen, approximately 3/5 are of mixed climb character (considering the lengths of the dislocation segments).

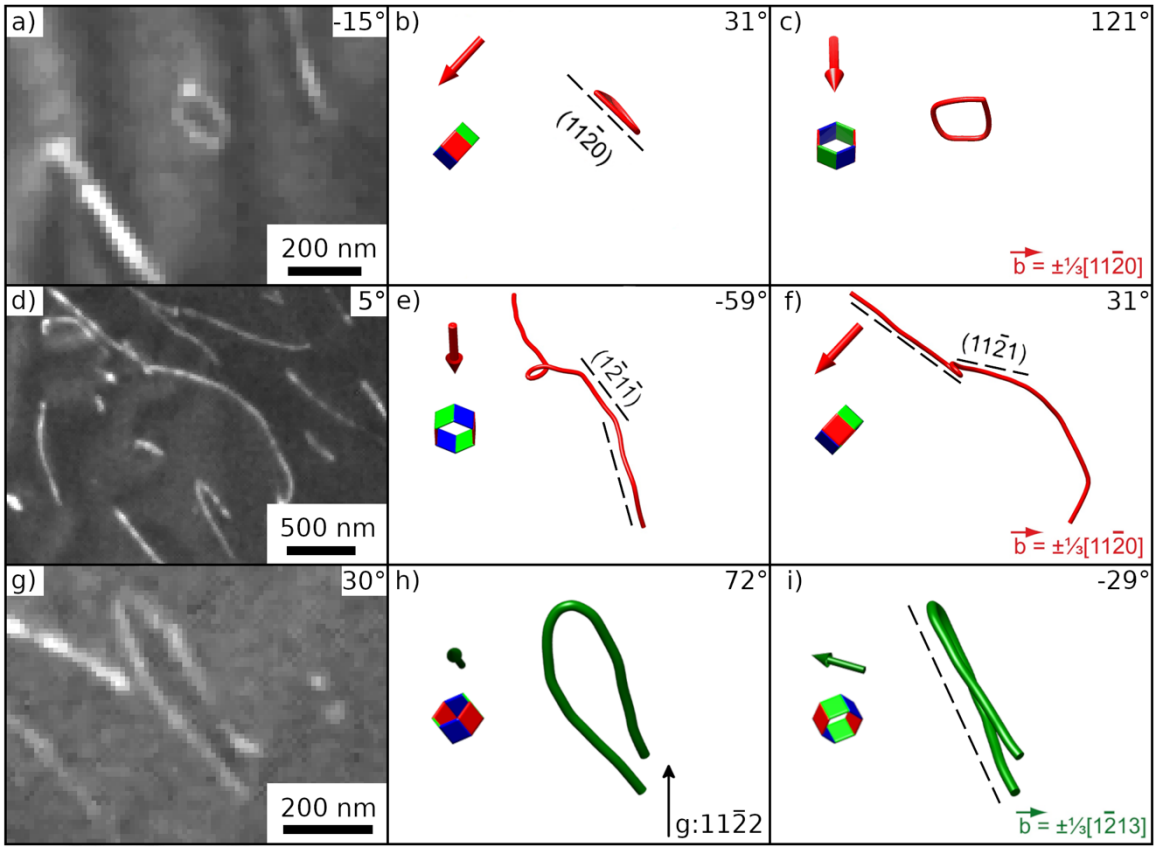

Figure 6: Climb characterizations revealed by dislocation electron tomography, obtained with the $11\bar{2}2$ diffraction vector, for specimen MCT: a) Raw WBDF micrograph of a $\boldsymbol{a_3}$ dislocation observed along a projection angle of -15°; b) reconstructed volume of this dislocation (coloured in red) for a projection angle of 31° where the prismatic $(11\bar{2}0)$ plane is edge-on; c) same reconstructed dislocation with a projected angle of 121°; d) raw WBDF micrograph of another geometrically complex $\boldsymbol{a_3}$ dislocation observed along a projection

angle of 5°; e) reconstructed volume of this dislocation for a projection angle of -59° where the pyramidal $(1\bar{2}1\bar{1})$ plane is edge-on; f) the same dislocation with a projected angle of 31° where the pyramidal $(11\bar{2}1)$ plane is edge-on; g) raw WBDF micrograph of a $\boldsymbol{c}-\boldsymbol{a_2}$ dislocation observed along a projection angle of 30°; h) the reconstructed volume of this dislocation (coloured in dark green) for a projection angle of 72°; i) the same reconstructed dislocation with a projected angle of -29° for which its plane is edge-on. The $\frac{1}{3}[11\bar{2}0](11\bar{2}0)$ pure climb system and the $\frac{1}{3}[11\bar{2}0](11\bar{2}1)$ and $\frac{1}{3}[11\bar{2}0](1\bar{2}1\bar{1})$ mixed climb systems have been characterized in this Figure. (For interpretation of the references to colour in this figure legend, the reader is referred to the web version of this article.)

3.3.2 MT specimen

We find the same results for the MT specimen as for the MCT specimen, with a significant proportion (around half) of dislocations in mixed climb configurations. (Figures 7d-f and 7g-i). An example of a small dislocation loop in a pure climb configuration has also been found (Figures 7a-c).

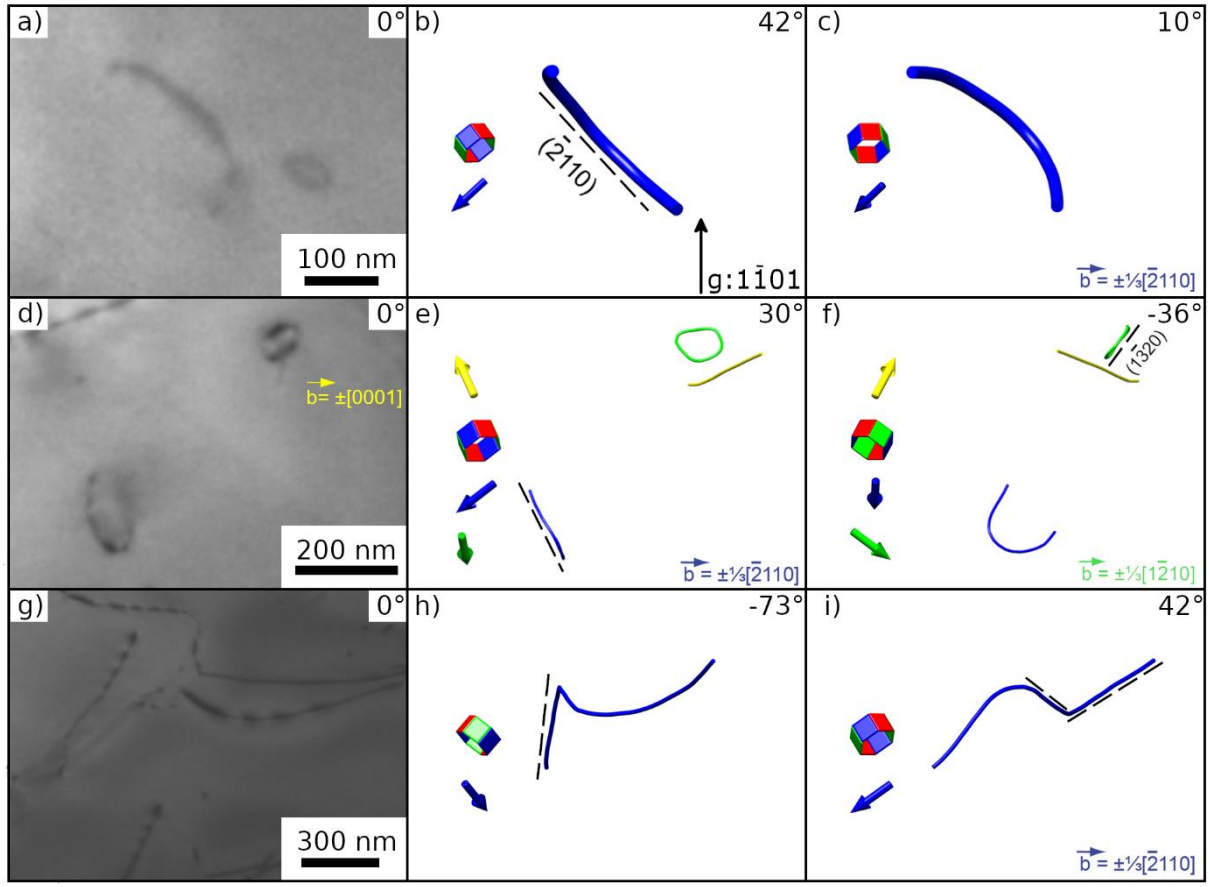

Figure 7: Characterizations of dislocation climb revealed by dislocation electron tomography, obtained with the $1\bar{1}01$ diffraction vector, for the MT specimen: a) Raw WBDF micrograph of a $\boldsymbol{a_1}$ dislocation observed along a projection angle of 0°; b) reconstructed volume of this dislocation (coloured in blue) for a projection angle of 42° for which the prismatic $(\bar{2}110)$ plane is edge-on; c) same reconstructed dislocation with a projected angle of 10°; d) raw WBDF micrograph of $\boldsymbol{a_1}$, $\boldsymbol{a_2}$ and $\boldsymbol{c}$ dislocations observed along a projection angle of 0°; e) reconstructed volume of these dislocations (coloured in blue, green and yellow respectively) for a projection

angle of 30° where the habit plane of the $\boldsymbol{a_1}$ dislocation loop is edge-on; f) same reconstructed dislocations with a projected angle of -36° where the prismatic $(1\bar{3}20)$ plane is edge-on (corresponding to the habit plane of the $\boldsymbol{a_2}$ dislocation loop); g) raw WBDF micrograph of a $\boldsymbol{c-a_2}$ complex dislocation observed along a projection angle of 0°; h) reconstructed volume of this dislocation for a projection angle of -73° where the habit plane of a part of this dislocation is edge-on; i) same reconstructed dislocation with a projected angle of 42° where the last two parts of this dislocation are edge-on. The $\frac{1}{3}[\bar{2}110](\bar{2}110)$ pure climb system and the $\frac{1}{3}[1\bar{2}10](1\bar{3}20)$ mixed climb system have been characterized in this figure. (For interpretation of the references to colour in this caption, the reader is referred to the web version of this article.)

3.4 Strain analysis from electron tomography data

The plastic strain inferred for the motion of each dislocation segment has been calculated based on the relations provided in section 2.4. We have considered, for each specimen, 1) the segments that correspond to pure glide ($\theta = 0$) only, 2) the segments in pure climb configurations ($\theta = 90°$) only, 3) all glide components of the segments (*i.e.* including pure glide segments and the glide contribution of segments in mixed climb configurations), and 4) all climb components (*i.e.* pure climb segments and the climb contributions of segments in mixed climb configurations). In all cases except in the case of pure climb, the set of available dislocations is sufficient to provide five independent strain components at the grain scale. Thus, the observed dislocation microstructure can accommodate any deformation. The Schmid tensors, either for glide or for climb, are full matrices in which no specific component dominates. The associated equivalent Schmid tensors, $\bar{S}^g_{eq} = \left(\bar{S}^g_{ii}\right)^{\frac{1}{2}}$ for all glide contributions and $\bar{S}^c_{eq} = (\bar{S}^c_{ii})^{\frac{1}{2}}$ for all climb contributions, have similar values, about 0.2 for MT for both glide and climb. Somewhat smaller values are obtained for glide (~0.1) than for climb (~0.4) for the MCT specimen.

4 Discussion

4.1 Slip systems

In our specimens, dislocations observed are mostly of the $\langle a \rangle$ and $\langle c+a \rangle$ types with only few [c] dislocations observed in the MT specimen. Active slip systems in quartz have been constrained by many experimental studies (Hobbs 1968, Baeta & Ashbee 1969, Morrison-Smith et al. 1976) and their activities have been shown to depend strongly on temperature. Below 700°C, $\langle a \rangle$ basal glide dominates. Above 700°C, glide becomes progressively more active in pyramidal ($\{1\bar{1}0n\}$ with n=0, 1, 2, 3), and then on prismatic planes. Above 750 °C, $\langle c+a \rangle$ dislocations are activated which glide in $\{1\bar{1}01\}$ and $\{11\bar{2}n\}$ with n=1, 2 and then [c]

glide on prism planes. Under geological conditions of strain-rate and deviatoric stress, the same sequence is assumed to be valid with the activation of [c] glide starting at 600-650 °C (Mainprice et al. 1986, Okudaira et al. 1995). Mainprice et al. (1986) also point out that the activation of [c] glide is favoured by wet conditions, which is the case in our specimens. Our observations are thus consistent with this transition sequence where $\langle a \rangle$ basal glide is not active, [c] glide is of marginal importance, and $\langle a \rangle$ slip occurs predominantly on pyramidal and prismatic planes. The only remarkable observation is the widespread activation of $\langle c + a \rangle$ glide in the $\{10\bar{1}0\}$, $\{10\bar{1}1\}$, $\{11\bar{2}n\}$ (n=1,2) and even $\{21\bar{3}1\}$ (not previously reported) planes. Glide along $\langle c + a \rangle$ is generally expected at high temperatures (Baeta & Ashbee 1969). However, while $\langle c + a \rangle$ glide is reported in the literature, it has been the subject of far fewer detailed observational studies than $\langle a \rangle$ and [c] glide, particularly in natural specimens. We had previously observed $\langle c + a \rangle$ dislocations in a Bohemian granulite (Mussi et al. 2021b). Yet in many studies that depend on extracting geometrically necessary dislocation densities from EBSD measurements (Wallis et al. 2019) or modelling crystal preferred orientations (e.g. Keller & Stipp 2011, Morales et al. 2011), <a + c> glide has been neglected. General strains can be explained by assuming activation of other systems, but such suppositions are contrary to the results of this study.

4.2 Mixed climb

The most important observation of this study is the significant activation of climb over a wide range of middle to deep crustal temperatures and tectonic strain rates. Besides some evidence for dislocations in pure climb configuration, we found pervasive evidence of mixed climb (Carrez et al. 2024) of $\langle a \rangle$ and $\langle c + a \rangle$ dislocations. The long-standing problem of achieving general strains and satisfying the von Mises-Taylor criterion can be solved for quartz either by activation of $\langle c + a \rangle$ glide, or climb. We show here that both operate together with $\langle c + a \rangle$ dislocations that exhibit mixed climb geometries. Moreover, we show that the contribution of glide produced by the observed microstructures is sufficient to satisfy the von Mises-Taylor criterion. Hence, activation of climb is not necessary to provide additional strain components, but it contributes to the magnitudes of strains achieved.

Activation of dislocation climb in quartz has been recognized for many decades (White 1977), especially under wet conditions when internal water contents exceed the solubility limit of water-related defects (Kirby & McCormick, 1979; Cordier & Doukhan 1989; McLaren et al. 1989). Climb is generally inferred by the absence of apparent lattice friction (curved and entangled dislocations) and by the presence of sub-grain boundaries (Baeta & Ashbee 1973;

Ball & Glover 1979), as found in our two specimens. It is always considered a recovery mechanism (Tullis & Yund 1989). Indeed, dislocation creep is usually described within the framework of Weertman (1968) creep where the strain is produced by dislocation glide whose resulting hardening is counterbalanced by a recovery mechanism, generally involving dislocation climb. It is implicit that dislocation glide produces most of the strain, while climb produces little strain but controls the strain-rate. This means that the glide velocity is supposed to be much greater (several orders of magnitude greater) than the climb velocity. On this basis, Boioli et al. (2015) modelled creep in olivine above 1400 K with a glide velocity more than a thousand times faster than the climb velocity under low stress.

Our observation of pervasive mixed glide and climb with movement planes taking any orientation between pure glide and pure climb in quartz mylonites of the MT and MCT (Figure 8) suggests that velocities of dislocation glide and climb were comparable. In this case, climb and glide are both strain-producing mechanisms. Deformation microstructures of γ-TiAl alloys deformed at 770-790°C led to the same observation, with a transition in the temperature/strain-rate domain where climb can reach the velocity of glide (Malaplate et al., 2004: Couret, 2010; Voisin et al., 2016; Galy et al. 2023). Preferential mixed climb has also been characterized in minerals such as olivine (Mussi et al., 2017) and MgO (Mussi et al., 2021a). Such mixed climb motions may be difficult to recognize without the characterization of both Burgers vectors and dislocation lines. However, we may well wonder whether this mechanism can be inferred from less detailed observations.

Early studies of deformation lamellae in quartz deformed in laboratory experiments (Christie et al., 1964; Hobbs, 1968; Tullis et al., 1973; Blacic, 1975) and under natural, crustal conditions (e.g., Sylvester, 1969; McLaren & Hobbs, 1972) were taken as evidence of slip on basal and prismatic planes. However, these planar optical features commonly occur at angles of up to 15-30^{o} from rational crystallographic planes perpendicular and parallel to c (Hobbs, 1968; Heard & Carter, 1968; Tullis et al., 1973; Christie & Ardell, 1974). Characterized optically by their anomalous refractive index, deformation lamellae observed by TEM were found to consist of lamellar zones of highly tangled dislocations rather than simple arrays of free dislocations in their anticipated slip planes (Christie & Ardell, 1976). Detailed TEM diffraction analysis of the tangled dislocations within these lamellae has not been possible. Nevertheless, Venooij (2005) posed the hypothesis that orientations of deformation lamellae, like slip bands, reveal directions of dislocation motion, and therefore give relative velocities of glide within basal and prism planes, and climb out of these planes. Heard & Carter (1968) showed that non-basal deformation lamellae are favoured by high temperature (and low strain

rate), as may be expected for higher climb velocities at higher temperatures. Misorientations of deformation lamellae may therefore result from some climb accompanying glide. Still, the tangled nature of dislocations within lamellar regions of early experiments indicates that climb was insufficient for significant recovery.

Much higher rates of dislocation climb and recovery are evident from the microstructures of MT and MCT quartzites and the DET analyses of this study. Compiling our results for these natural quartz shear zone specimens, Table 1 summarizes length-weighted proportions of dislocations found in glide, pure climb, and mixed glide-climb orientations.

		MCT specimen		MT specimen	
Without straight dislocation segments	% Glide	9		16	
	% Pure climb	1	91	3	84
	% Mixed climb	90		81	
With straight dislocation segments	% Glide	38		51	
	% Pure climb	1	62	2	49
	% Mixed climb	61		47	

Table I: Proportion of dislocation segments in glide, pure climb and mixed climb configuration for each specimen, depending on whether or not straight segments are included in the counting.

Glide-producing dislocation lines constitute *ca.* 38 % of the total in the MCT specimen and approximately 50 % for the MT specimen. More than half of the total dislocation line lengths analyzed involve some climb (pure or mixed) component in both specimens. Considering the length of each dislocation segment and measuring the angle between Burgers vector and normal vector to each plane of motion $(\widehat{n,b})$, histograms can be plotted for all dislocation segments to quantify the climb contribution for each kind of Burgers vector. The $(\widehat{n,b})$ angle ranges from 0° for pure climb to 90° for glide configurations (see Figure 8). Figures 8a and 8c describe the climb distribution of the MCT specimen without and with rectilinear dislocation

segments respectively. Similarly Figures 8b and 8d show the climb distributions for MT specimens without and with rectilinear dislocation segments, respectively. These histograms show no significant difference between dislocation microstructures in specimens MCT and MT. <a> dislocations are found most often in climb or mixed climb orientations.

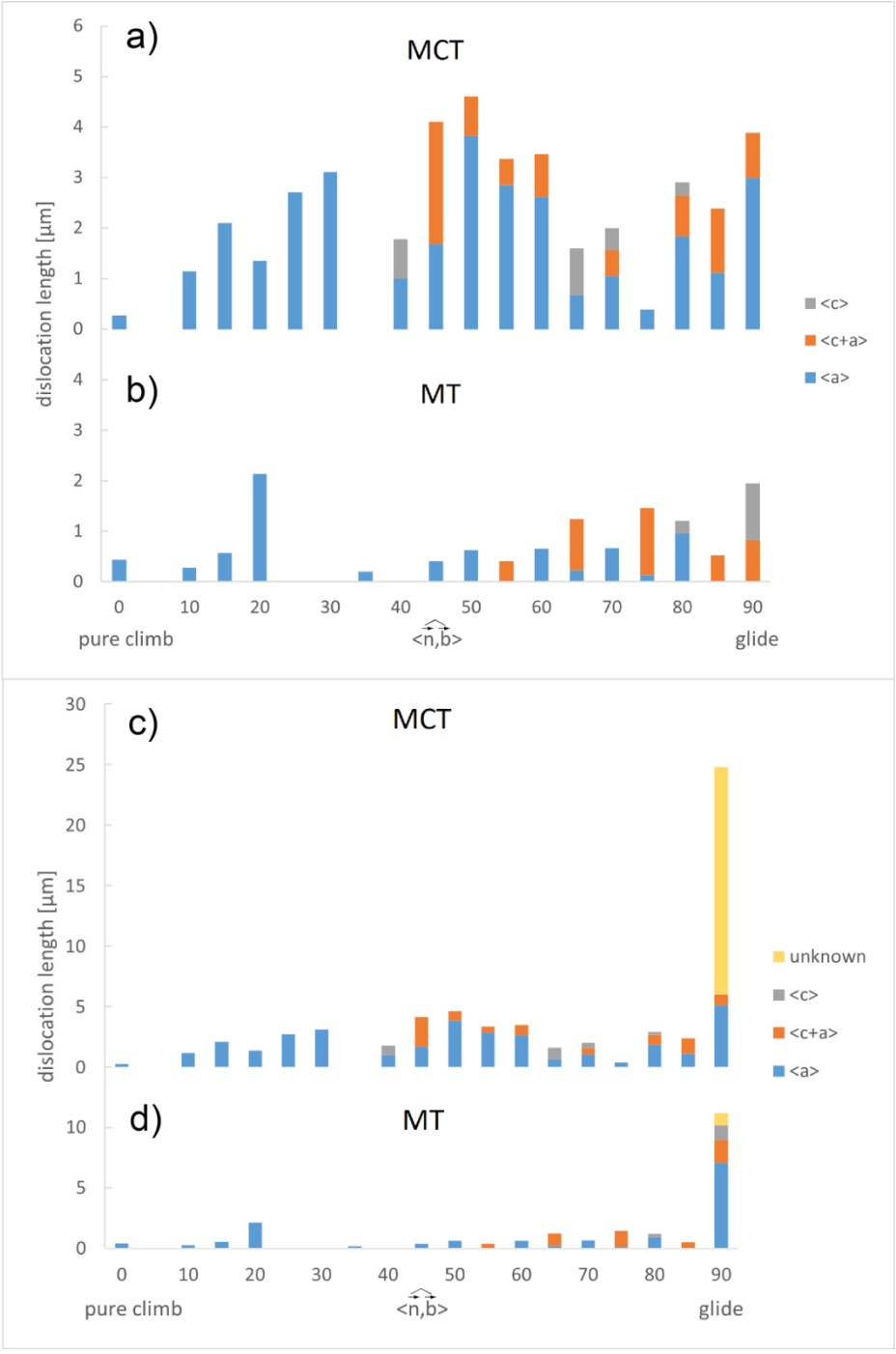

Figure 8: Histograms quantifying the climb contribution in quartz of <c>, <c+a>, and <a> dislocations: a) Histogram of the evolution of the angle between Burgers vectors and normal vectors to habit planes $(\widehat{n,b})$ normalized for dislocation segment lengths for the MCT specimen; b) histogram for the MT specimen; c) MCT specimen: histogram where the lengths of straight-line dislocation segments are included, considering these

segments are in a glide configuration; d) MT specimen: histogram where the lengths of straight-line dislocation segments are included. From these histograms, more than 50% of the dislocation length is found in climb configurations.

Our calculations (section 3.4) for both MT and MCT specimens indicate that plastic strains produced by climb are of the same order of magnitude (possibly larger for the MCT specimen) as produced by glide.

This is an important observation, as it as it bears on interpretations of CPO of rock deformed by dislocation creep. In recent studies, deformation is taken to be due to glide on the $\langle a \rangle$ basal system, then $\langle a \rangle$ prismatic/pyramidal slip, and then [c] prismatic slip with increasing temperature (Okudaira et al. 1995, Keller & Stipp, 2011, Morales et al. 2011, 2014, Tokle et al. 2019). Changes in proportions of different slip systems activated at different temperatures and strain rates are presumably reflected in c-axis fabrics of quartz mylonites, with an opening angle about the normal to foliation for pure shear that constitutes a balance between slip systems that rotate c-axes towards the maximum compressive stress (normal to foliation) and those that rotate c-axes towards foliation. Conceptual and numerical models of CPO development (e.g., Tullis et al., 1973; Lister & Hobbs, 1980; Wenk et al., 1989, 2019) are based on varying proportions of dislocation glide on <a> basal, <a> prism, <a> pyramidal, [c] prism, and <c+a> pyramidal systems, but we know of no models that incorporate <c+a> prism glide or climb as a strain mechanism. Revisions in our interpretation of CPO will need to include the additional slip system with displacement vector <c+a>. Kinematically, adding <c+a> glide will alter the proportions of <a> and [c] glide. Moreover, if only glide is considered, we will miss a significant fraction of strains during dislocation creep.

Deformation thermometers such as the quartz c-axis fabric opening angle thermometers of Kruhl (1998) and Faleiros et al. (2016) do not explicitly take into account the separate potential influences of glide and climb on fabric development. However, the interpretation of these empirically based thermometers will depend on activation of slip systems at varying temperature, strain rate and action of hydrous defects. Relations between glide-induced CPO and total strain will further depend on how much strain is accomplished by glide and by climb.

4.4 Inferring stress loading

Sylvester (1969) suggested that deviations of deformation lamellae orientations from rationale crystallographic planes tend towards planes of high shear stress, potentially offering a tool to reconstruct internal stresses. Here, we explore this hypothesis further. To do this, we represent

on Figure 9 the different systems (glide or climb) on a stereographic projection for quartz with positive vertical $[0001]$ (upper hemisphere). Figure 9a summarizes our observations for the different types of dislocations, color-coding the contribution of climb. From this stereographic projection (Figure 9b), we can see that the orientation of the grain analysed in the MCT specimen strongly enhances activation of the $\frac{1}{3}[1\bar{2}10](10\bar{1}0)$ glide system. As a result, there is little climb of $\frac{1}{3}[1\bar{2}10]$ dislocations. In contrast, glide of $\frac{1}{3}[11\bar{2}0]$ dislocations is less favourable (Fig. 9c) increasing the tendency to climb. In Figure 9d, we extract the glide components of the mixed climb planes of $\frac{1}{3}[11\bar{2}0]$ dislocations into the pure climbing plane normal (along the $[11\bar{2}0]$ direction), but also on the glide plane normal depicted in Figure 1. This allows us to highlight a high contribution of two easy slip systems: $\frac{1}{3}[11\bar{2}0](\bar{1}100)$, $\frac{1}{3}[11\bar{2}0](\bar{1}101)$ and, to a lesser extent, of $\frac{1}{3}[11\bar{2}0](\bar{1}10n)$ as well as some other unexpected planes. Such evidence of glide in planes that have not been reported for quartz raises questions. Dislocation motion in these planes does not correspond to pure glide, but is associated with mixed climb. This observation is in line with the interpretation made by Malaplate et al. (2004) of mixed climb in TiAl alloys. According to them, dislocation motion in mixed climb planes may be facilitated by reduced lattice friction during pure glide (probably linked to specific dislocation core structures). We hypothesize that activation of mixed glide and climb may allow activation of glide on additional planes. This hypothesis, based as it is on preliminary observations, requires further observational and theoretical investigation.

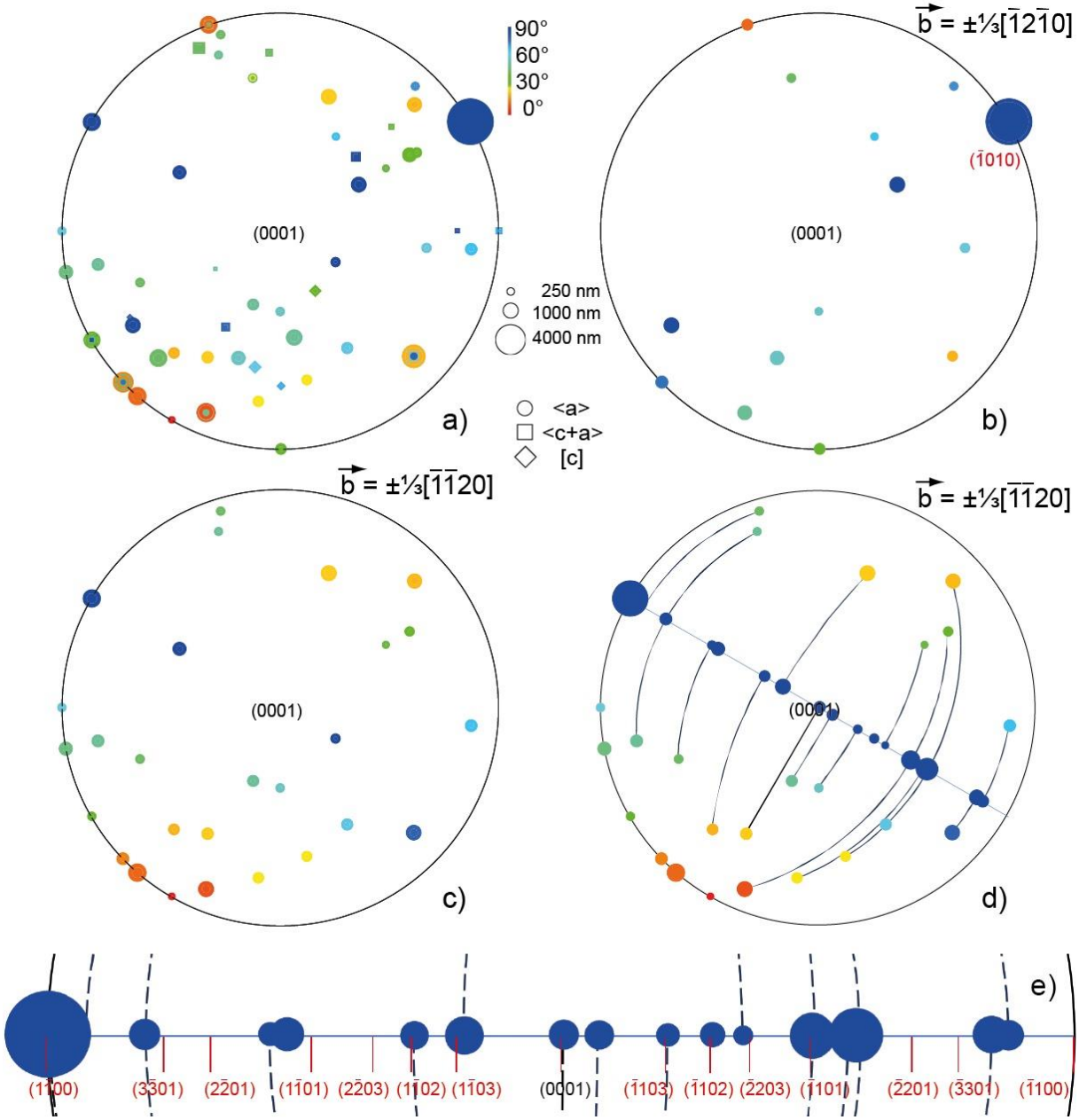

Figure 9: (0001) stereographic projection (upper hemisphere) of the normal to the habit planes of dislocations characterized in the MCT specimen. The rainbow colour code is associated with the angle between the habit plane normal and the Burgers vectors (0° in red for pure climb and 90° in blue for glide) and the symbol sizes correspond to the lengths of dislocations using a non-linear scale illustrated by three examples: 250, 1000 and 4000 nm. a) All Burgers vectors are represented ($\langle a \rangle$ dislocations are represented by circles, $\langle c + a \rangle$ by squares and $[c]$ by diamonds); b) Projections of the habit plane normals for $\boldsymbol{a_2}$ dislocations (a high proportion of dislocations found in the $(\bar{1}010)$ glide plane); c) Projections of habit plane normal for $\boldsymbol{a_3}$ dislocations (a few in glide planes and many in mixed climb configurations); d) Stereographic projection for $\boldsymbol{a_3}$ dislocations where the glide components of the mixed climb planes are extracted and added. These glide components are linked to their parent mixed climb plane by a solid line. e) enlargement of the layer of d) showing glide planes normal to the plane Miller indices in the quartz structure to show the diversity of glide components involved.

We have also applied the method described in section 2.5.3 to learn whether the stress state that acted *in situ* can be inferred. Several minimization attempts have been carried out, and slightly better results have been obtained when allowing different slip resistances τ_0 for dislocations with $\langle a \rangle$, $\langle c+a \rangle$, and $[c]$ Burgers vectors. Results (Figure 10 for MT) show a good match between the observed and computed θ values. In the minimization procedure, we had to optimize not only the stress state but also the rheological parameters. Best results are obtained for a nearly linear behavior for both glide and climb ($n_g \approx n_c \approx 1$) and slip resistance for $\langle c+a \rangle$ and [c] dislocations just half the slip resistance for $\langle a \rangle$ dislocations.

The stress state obtained in this way for the MT specimen (Figure 11) indicates that the larger normal stress (promoting climb) was along directions close to $\langle c+a \rangle$ and that the maximum shear stress (promoting glide) appeared to be on planes close to $\{10\bar{1}0\}$ or to (0002). Another graphical representation of the stress state inferred in the MT specimen is the stress ellipsoid (Figure 12 and Supplementary movie). It exhibits an oblate shape, two principal stresses having similar absolute values (-4.4 and 5.2) while the third one is significantly smaller (0.8). The stress ellipsoid, oriented along the TEM view direction, is represented in Figure 2.

While this estimation of the local stress state acting *in situ* does not take into account changes in stress during the plastic deformation history, it is, to our knowledge, the first estimation of *in situ* stress state based on observed dislocation structures. Moreover, the rheological coefficients thus obtained for MT and MCT shear zones correspond to *in situ* conditions and extremely slow geological strain-rates.

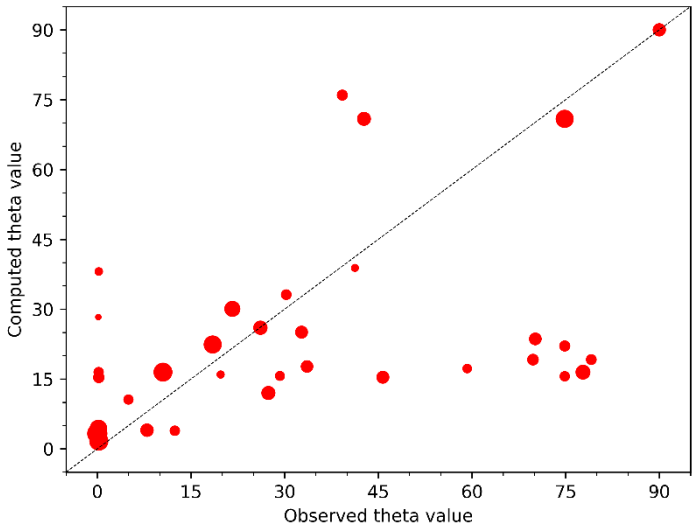

721 **Figure 10.** Computed θ^{mod} angles vs. observed θ^{obs} angles after minimizing the objective function (13) to find
722 the stress state that is most consistent with the observations, for specimen MT. Each symbol corresponds to a
723 different dislocation segment, and their size is proportional to the segment length.
724
725

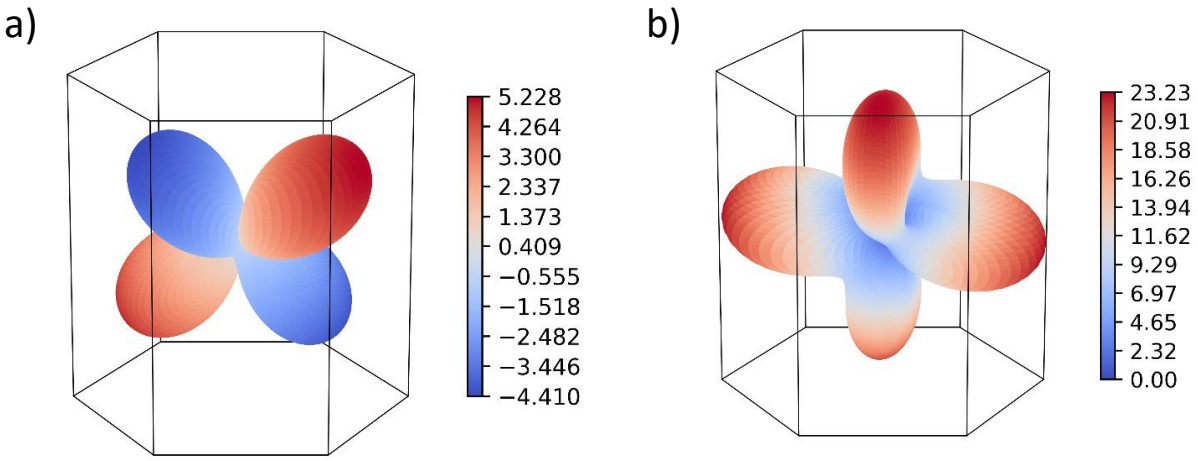

726
727 **Figure 11.** Stress state obtained for specimen MT after minimization of (13), plotted with respect to the
728 hexagonal crystal lattice. (a) Norm of the normal stress acting on specific crystallographic planes, for any
729 possible plane orientation. (b) Norm of the shear stress acting on those crystallographic planes. Stress values are
730 relative, and adimensional, normalized by the critical shear stress corresponding to <a> glide.
731

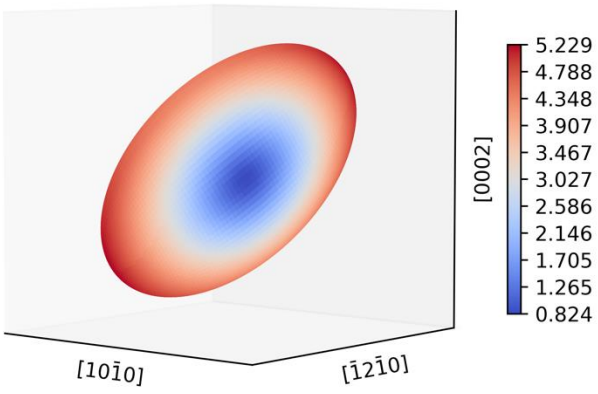

732
733 **Figure 12.** Lamé's stress ellipsoid for specimen with respect to crystallographic directions of the quartz grain of
734 the MT specimen. Among the three principal stresses, two have similar absolute values (-4.4 and 5.2) while the
735 third one is significantly smaller (0.8) resulting in an oblate shape. Stress values are relative, and adimensional,
736 normalized by the critical shear stress corresponding to <a> glide. See also Supplementary movie.
737

738 ## 5 Conclusion

739 This study involves two specimens of quartz deformed in two natural shear zones from the
740 Moine and Main Central thrusts, both of which were deformed extensively by dislocation
741 creep in the presence of water. We show that $\langle a \rangle$ slip occurs predominantly on pyramidal and

prismatic planes, that $\langle a \rangle$ basal glide is not active, and that [c] glide is not significant under those conditions. A remarkable observation is the widespread activation of $\langle c + a \rangle$ glide in the $\{10\bar{1}0\}$, $\{10\bar{1}1\}$, $\{11\bar{2}n\}$ (n=1,2) and even $\{21\bar{3}1\}$ (not previously reported) planes. Even more remarkable is the conclusion that more than approximately 60 % of all dislocations involve climb in their motion. This result could only be realized through characterization of the three-dimensional microstructure of the dislocation lines by electron tomography. The simultaneous motion of dislocations by glide and climb, known as mixed climb in materials science, is apparently widespread in naturally deformed quartz shear zones. This mode of deformation is characterized by displacement of dislocations in intermediate planes between the glide plane and the climb plane, with significant implications for relative glide velocity v_g and climb velocity v_c; v_g and v_c must have comparable magnitudes under natural strain rates. Our quantitative characterization of slip systems in these samples demonstrates that glide of the observed dislocations can satisfy the von Mises-Taylor criterion. Hence, activation of climb is not necessary to provide additional strain components. On the other hand, the magnitudes of strains achieved include contributions due to dislocation climb. Plastic strains produced by climb are not subordinate to those of glide; rather, they are of the same order of magnitude as strains due to glide (and possibly larger for the MCT specimen). Strain analysis based on the exclusive activation of glide systems does not therefore provide a satisfactory description of quartz deformation at natural strain rates. In this study, we also present a preliminary attempt to model the local stress field that may be the cause of the observed microstructure. We show that, in at least one case, microstructure analysis appears to constrain the mechanical conditions that acted *in situ*.

Acknowledgements

This project has received funding from the European Research Council (ERC) under the European Union's Horizon 2020 research and innovation program under grant agreement 787198 – TimeMan. The Chevreul Institute is thanked for its help in the development of this work through the ARCHI-CM project supported by the "Ministère de l'Enseignement Supérieur de la Recherche et de l'Innovation", the region "Hauts-de-France", the ERDF program of the European Union and the "Métropole Européenne de Lille". The electron microscopy facility of the Chevreul Institute is also supported by the INSU.

Author contributions (CRediT taxonomy):

Conceptualization: TW, AM, AK, RL and PC; Formal analysis TW, AM, OC; Funding acquisition PC; Investigation TW, AM; Methodology AM, OC; Resources AK, RL; Software OC; Supervision PC; Validation AM; Visualization TW, AM, OC; Writing – original draft TW, AM, OC, AK, RL, PC; Writing – review & editing TW, AM, OC, AK, RL, PC

780 **Data availability:**
781 Raw data are available at: https://zenodo.org/doi/10.5281/zenodo.10635127

References

Baëta, R.D., & Ashbee, K.H.G. (1969). Slip systems in quartz: I experiments. *American Mineralogist* 54, 1551–1573.

Baëta, R.D., & Ashbee, K.H.G. (1973). Transmission electron microscopy studies of plastically deformed quartz. *Physica Status Solidi (a)* 18, 155-170. https://doi.org/10.1002/pssa.2210180112

Bakker, R.J., & Jansen, J.B.H. (1990). Preferential leakage from fluid inclusions by means of mobile dislocations, *Nature*, 345, 58-60.

Bakker, R.J., & Jansen, J.B.H. (1994) A mechanism for preferential H_2O leakage from fluid inclusions in quartz, based on TEM observations, *Contributions to Mineralogy and Petrology*, 116, 7-20.

Ball, A., & Glover, G. (1979). Dislocation climb deformation in quartz. *Bulletin de Minéralogie* 102, 188-194. https://doi.org/10.1007/BF00308119.

Ball, A., & White, S. (1978). On the deformation of quartzite. *Physics and Chemistry of Minerals* 3, 163–172. https://doi.org/10.1007/BF00308119.

Barnard, J.S., Sharp, J., Tong, J.R. & Midgley, P.A. (2006). High-resolution three-dimensional imaging of dislocations. *Science* 313, 319. https://www.science.org/doi/10.1126/science.1125783

Blacic, J.D. (1975). Plastic deformation mechanisms in quartz: the effect of water. *Tectonophysics* 27, 271–294. https://doi.org/10.1016/0040-1951(75)90021-9

Behrmann, J.H., & Mainprice, D.H. (1987). Deformation mechanisms in a high temperature quartz-feldspar mylonite: evidence of superplastic flow in the lower continental crust. *Tectonophysics* 140, 297–305. https://doi.org/10.1016/0040-1951(87)90236-8

Boioli, F., Carrez, P., Cordier, P., Bevincre, B., & Marquille, M. (2015). Modeling the creep properties of olivine by 2.5-dimensional dislocation dynamics simulations. *Physical Review B.* 92, 014115. http://dx.doi.org/10.1103/PhysRevB.92.014115

Carrez, P., Mussi, A. & Cordier, P. (2024) On dislocation climb as an important deformation mechanism for planetary interiors. *Annual Review of Earth and Planetary Sciences*, 52, in press, https://doi.org/10.1146/annurev-earth-031621-063108

Castelnau, O., Derrien, K., Ritterbex, S., Carrez, P., Cordier, P. & Moulinec, H. (2020). Multiscale modeling of the effective viscoplastic behavior of Mg_2SiO_4 wadsleyite: bridging atomic and polycrystal scales. *Comptes Rendus de Mécanique*, 10-11, 827–846.

Christie, J.M., & Ardell, A.J. (1974). Substructures of Deformation Lamellae in Quartz. *Geology* 2 (8), 405–408. https://doi.org/10.1130/0091-7613(1974)2<405:SODLIQ>2.0.CO;2

Christie, J.M., & Ardell, A.J. (1976). Deformation Structures in Minerals. In: Wenk, H.R. (ed.) Electron Microscopy in Mineralogy. Springer, Berlin, Heidelberg. https://doi.org/10.1007/978-3-642-66196-9_29

Christie, J.M., Heard, H.C., & LaMori, P.N. (1964). Experimental deformation of quartz single crystals at 27 to 30 kilobars confining pressure and 24°C. *American Journal of Science*, 262, 26-55.

Cordier, P., Boulogne, P. & Doukhan, J.C. (1988). Water precipitation and diffusion in wet quartz and wet berlinite $AlPO_4$. *Bulletin de Minéralogie*, 111, 113–137.

Cordier, P., & Doukhan, J.C. 1989. Water solubility in quartz and its influence on ductility. *European Journal of Mineralogy* 1, 221-237. doi: 10.1127/ejm/1/2/0221

Cordier, P. & Doukhan, J.-C. (1991). Water speciation in quartz: a near infrared study, *American Mineralogist*, 76, 361-369.

Cotton, J.D. & Kaufman, M.J. (1991). A simplified method for determining the number of independent slip systems in crystals. *Scripta Metallurgica and Materialia*, 25, 2395–2398, https://doi.org/10.1016/0956-716X(91)90036-Z

Couret A. (2010). Low and high temperature deformation mechanisms in TiAl Alloys. J. Phys.: Conf. Ser. 240:012001. https://doi.org/10.1088/1742-6596/240/1/012001

De Ridder, R. & Amelinckx, S. (1971). Approximate theoretical treatment of weak-beam dislocation images. *Physica Status Solidi* 43, 541–550. https://doi.org/10.1002/pssb.2220430211.

Doukhan, J.C. & Trépied, L. (1985). Plastic deformation of quartz single crystals. *Bulletin de Minéralogie* 108, 97-123. https://doi.org/10.3406/bulmi.1985.7860.

Doukhan, J.-C., & Paterson, M.S. (1986) Solubility of water in quartz - a revision, *Bulletin de Minéralogie*, 109, 193-198.

Faleiros, F.M., Moraes, R., Pavan, M. & Campanha, G.A.C. (2016). A new empirical calibration of the quartz c-axis fabric opening-angle deformation thermometer. *Tectonophysics*, 671, 173-182, https://doi.org/10.1016/j.tecto.2016.01.014

Francsis, M.K., (2012). Piezometry and strain rate estimates along mid-crustal shear zones. Unpublished MS thesis, Virginia Tech, USA, https://vtechworks.lib.vt.edu/handle/10919/32170

Fliervoet, T., White, S., & Drury, M.R. (1997). Evidence for dominant grain-boundary sliding deformation in greenschist-and amphibole-grade polymineralic ultra mylonites from the Redbank Deformed Zone, Central Australia. *Journal of Structural Geology* 19, 1495–1520. https://doi.org/10.1016/S0191-8141(97)00076-X

Fukuda, J.-I., Holyoke III, C.W. & Kronenberg, A.K. (2018). Deformation of fine-grained quartz aggregates by mixed diffusion and dislocation creep. *Journal of Geophysical Research Solid Earth* 123, 4676–4696. https://doi.org/10.1029/2017JB015133.

Galy B, Musi M, Hantcherli M, Molénat G, Couret A, Spoerk-Erdely P, Clemens H, & Monchoux JP. (2023). Glide and mixed climb dislocation velocity in γ-TiAl investigated by in-situ transmission electron microscopy. *Scripta Materialia*, 228 :115333. https://doi.org/10.1016/j.scriptamat.2023.115333

Gerretsen, J., Paterson, M.S., & McLaren, A.C. (1989). The uptake and solubility of water in quartz at elevated pressure and temperature, *Physics and Chemistry of Minerals*, 16, 334-342.

Griggs, D.T. & Blacic, J.D. (1965). Quartz: anomalous weakness of synthetic crystals, *Science*, 147, 292-295. https://www.science.org/doi/10.1126/science.147.3655.292

Griggs, D. (1967). Hydrolytic weakening of quartz and other silicates, *Geophys. J. R. Astron. Soc.*, 14(1–4), 19–31. https://doi.org/10.1111/j.1365-246X.1967.tb06218.x

Griggs, D. (1974). A model of hydrolytic weakening in quartz. *Journal of Geophysical Research* 79, 1653-1661. https://doi.org/10.1029/JB079i011p01653

Hata, S., Miyazaki, H., Miyazaki, S., Mitsuhara, M., Tanaka, M., Kaneko, K., Higashida, K., Ikeda, K., Nakashima, H., Matsumura, S., Barnard, J.S., Sharp, J.H., & Midgley, P.A. (2011). High-angle triple-axis specimen holder for three-dimensional diffraction contrast imaging in transmission electron microscopy. *Ultramicroscopy* 111, 1168-1175.https://doi.org/10.1016/j.ultramic.2011.03.021

Heard, H. C., & Carter, N. L. (1968). Experimentally induced "natural" intragranular flow in quartz and quartzite: *American Journal of Science*, 266, 1-42. https://doi.org/10.2475/ajs.266.1.1

Heggie, M. (1992) A molecular water pump in quartz dislocations, *Nature*, 355, 337-339.

Heggie, M. & Jones, R. (1986). Models of hydrolytic weakening in quartz, *Philosophical Magazine A*, 53, L65-L70. https://doi.org/10.1080/01418618608242857

Heggie, M., Jones, R., & Nylen, M. (1985). Electronic structure of α-quartz, the [1010] surface and perfect stoichiometric dislocations, *Philosophical Magazine B*, 51, 573-580. https://doi.org/10.1080/13642818508243148

Herman, G.T., Lakshminarayanan, A.V., & Naparstek, A. (1976). Convolution reconstruction techniques for divergent beams. *Comput. Biol. Med*. 6, 259–271. https://doi.org/10.1016/0010-4825(76)90065-2

Hirsch, P.B. (1981). Plastic deformation and electronic mechanisms in semiconductors and insulators, *Journal de Physique Colloque* 42, C3-149-C3-160.

Hirth, G., Teyssier, C., & Dunlap, W.J. (2001). An evaluation of quartzite flow laws based on comparisons between experimentally and naturally deformed rocks. *International Journal of Earth Sciences*, 90, 77-87. https://doi.org/10.1007/s005310000152

Hirth, G. & Tullis, J. (1992). Dislocation creep regimes in quartz aggregates, *Journal of Structural Geology*, 14(2), 145–159. https://doi.org/10.1016/0191-8141(92)90053-Y

Hobbs, B.E. (1968). Recrystallization of single crystals of quartz. *Tectonophysics*. 6, 353-401. https://doi.org/10.1016/0040-1951(68)90056-5

Hobbs, B.E. (1981). The influence of metamorphic environment upon the deformation of minerals, *Tectonophysics*, 78, 335-383. https://doi.org/10.1016/0040-1951(81)90020-2

Hobbs, B.E. (1984). Point defect chemistry of minerals under a hydrothermal environment, *Journal of Geophysical Research*, 89, 4026-4038. https://doi.org/10.1029/JB089iB06p04026

Hodges, K.V. (2000). Tectonic of the Himalaya and southern Tibet from two perspectives. *Geological Society of America Bulletin*, 112, 324-350, https://doi.org/10.1130/0016-7606(2000)112<324:TOTHAS>2.0.CO;2

Holyoke, III, C.W. & Kronenberg, A.K. (2010). Accurate differential stress measurement using the molten salt cell and solid salt assemblies in the Griggs apparatus with application to strength, piezometers and rheology. *Tectonophysics*, 494, 17-31, https://doi.org/10.1016/j.tecto.2010.08.001

Ishida, Y., Ishida, H., Kohra, K. & Ichinose, H. (1980) Determination of the Burgers vector of a dislocation by weak-beam imaging in a HVEM. *Philosophical Magazine A* 42, 453–462. https://doi.org/10.1080/01418618008239369

Johnson, M.R.W., Kelley, S.P., Oliver, G.J.H., & Winter, D.A. (1985). Thermal effects and timing of thrusting in the Moine thrust zone. *Journal Geological Society London*, 142, 863-873. https://doi.org/10.1144/gsjgs.142.5.0863

Kekulawala, K.R.S.S, Paterson, M.S., & Boland, J.N. (1978). Hydrolytic weakening in quartz, *Tectonophysics*, 46, T1-T6. https://doi.org/10.1016/0040-1951(78)90101-4

Kekulawala, K.R.S.S, Paterson, M.S., & Boland, J.N. (1981). An experimental study of the role of water in quartz deformation, In: Carter, N.L., Friedman, M., Logan, J.M., Stearns, D.W. (Eds), Mechanical Behavior of Crustal Rocks (The Handin Volume), Geophysical Monograph 24, 49-60, Amer. Geophys. Union, Washington, D.C.

Keller, L.M., & Stipp, M. (2011). The single-slip hypothesis revisited: Crystal-preferred orientations of sheared quartz aggregates with increasing strain in nature and numerical simulation. *Journal of Structural Geology* 33, 1491-1500. https://doi.org/10.1016/j.jsg.2011.07.008

Kirby, S.H. & McCormick, K.W. (1979). Creep of hydrolytically weakened synthetic quartz crystals oriented to promote {2-1-10} <0001> slip: a brief summary of work to date, *Bulletin de Minéralogie*, 102, 124-137.

Kronenberg, A.K., Kirby, S.H., Aines, R.D., & Rossman, G.R. (1986) Solubility and Diffusional Uptake of Hydrogen in Quartz at High Water Pressures: Implications for Hydrolytic Weakening. *Journal of Geophysical Research*, 91, 12723-12744. https://doi.org/10.1029/JB091iB12p12723

Kronenberg, A.K., Hasnan, H.F.B., Holyoke III, C.W., Law, R.D., Liu, Z., & Thomas, J.B., (2017). Synchrotron FTIR imaging of OH in quartz mylonites. *Solid Earth*, 8, 1025-1045. https://doi.org/10.5194/se-8-1025-2017

Kronenberg, A.K., Ashley, K.T., Francsis, M.K., Holyoke III, C.W., Jezek, L., Kronenberg, J.A., Law, R.D., & Thomas, J.B. (2020). Water loss during dynamic recrystallization of Moine thrust quartzites, northwest Scotland. *Geology*, 48, 557–561, https://doi.org/10.1130/G47041.1

Kruhl, J. (1998). Reply: Prism- and basal-plane parallel subgrain boundaries in quartz: a microstructural geothermobarometer. *Journal of Metamorphic Geology* 16, 142-146.

Law, R.D. (2014). Deformation thermometry based on quartz c-axis fabrics and recrystallization microstructures: A review. *Journal of Structural Geology*, 66, 129-161, https://doi.org/10.1016/j.jsg.2014.05.023.

Law, R.D., Casey, M., & Knipe, R.J. (1986). Kinematic and tectonic significance of microstructures and crystallographic fabrics within quartz mylonites from the Assynt and Eriboll regions of the Moine thrust zone, NW Scotland. *Trans. Roy. Soc. Edinburgh: Earth Sciences*, 77, 99-125. https://doi.org/10.1017/S0263593300010774

Law, R.D., Mainprice, D., Casey, M., Lloyd, G.E., Knipe, R.J., Cook, B., & Thigpen, J.R. (2010). Moine Thrust zone mylonites at the Stack of Glencoul: 1 - microstructures, strain and influence of recrystallization on quartz crystal fabric development. *Geological Society, London, Special Publications*, 335, 543-577, https://doi.org/10.1144/SP335.23

Law, R.D., Stahr, D.W. III, Francsis, M.K., Ashley, K.T., Grasemann, B., & Ahmad, T. (2013). Deformation temperatures and flow vorticities near the base of the Himalayan Series, Sutlej Valley and Shimla Klippe, NW India. *Journal of Structural Geology*, 54, 21-53, https://doi.org/10.1016/j.jsg.2013.05.009

Law, R.D., Strachan, R.A., Thirlwall, M.F. & Thigpen, J.R. in press. The Caledonian orogeny: Late Ordovician to Early Devonian tectonic and magmatic events associated with closure of the Iapetus Ocean. In: Smith, M. & Strachan, R.A. (editors) *Geology of Scotland* (5th edition). Geological Society of London.

Lebensohn, R.A., Hartley, C.S., Tomé, C.N. & Castelnau, O. (2010). Modelling the mechanical response of polycrystals deforming by climb and glide. *Philosophical Magazine*, 90(5), 567–583. https://doi.org/10.1080/14786430903213320

Lister, G.S. & Hobbs, B.E. (1980). The simulation of fabric development during plastic deformation and its application to quartzite: the influence of deformation history, *Journal of Structural Geology*, 2, 355-370. https://doi.org/10.1016/0191-8141(80)90023-1 Get rights and content

Liu, G.S. & Robertson, I.M. (2011). Three-dimensional visualization of dislocation-precipitate interactions in a Al–4Mg–0.3Sc alloy using weak-beam dark-field electron tomography. *Journal of Materials Research* 26, 514–522. https://doi.org/10.1557/jmr.2010.83

Madec, R., Devincre, B., Kubin, L., Hoc, T. & Rodney, D. (2003) The Role of Collinear Interaction in Dislocation-Induced Hardening. *Science*, 301, 1879-1882. https://doi.org/10.1126/science.1085477

Mainprice, D., Bouchez, J.L., Blumenfeld, P., & Tubià, J.M. (1986). Dominant c slip in naturally deformed quartz: Implications for dramatic plastic softening at high temperature. *Geology*, 14, 819-822. https://doi.org/10.1130/0091-7613(1986)14<819:DCSIND>2.0.CO;2

Malaplate J, Caillard D, & Couret A. (2006). Interpretation of the stress dependence of creep by a mixed climb mechanism in TiAl. *Philosophical Magazine* 84, 3671-3687. https://doi.org/10.1080/14786430412331284009

McLaren, A.C., & Hobbs, B.E. (1972). Transmission electron microscope investigation of some natural deformed quartzites. In: Heard, H.C., Borg, I.Y., Carter, N.L., Raleigh, C.B. (Eds.). Flow and Fracture of Rocks. Am. Geophys. Union, Geophys. Monogr. Ser. 16, 55–66. https://doi.org/10.1029/GM016p0055

McLaren, A. C., Fitz Gerald, J.D. & Gerretsen, J. (1989). Dislocation nucleation and multiplication in synthetic quartz: Relevance to water weakening. *Physics and Chemistry of Minerals*, 16(5), 465–482. https://doi.org/10.1007/BF00197016

Messaoudi, C. Boudier, T., Sanchez Sorzano, C.O., & Marco, S. (2007). TomoJ: tomography software for three-dimensional reconstruction in transmission electron microscopy. BMC Bioinform. 8, 288. https://doi.org/10.1186/1471-2105-8-288

Morales L.F.G, Mainprice D, Lloyd GE, & Law R.D. (2011). Crystal fabric development and slip systems in a quartz mylonite: an approach via transmission electron microscopy and viscoplastic self-consistent modelling. *Geol. Soc. London, Special Pub.*, 360, 151–174. https://doi.org/10.1144/SP360.9

Morales, L.F.G., Lloyd, G.E., & Mainprice, D. (2014). Fabric transitions in quartz via viscoplastic self-consistent modeling part I: axial compression and simple shear under constant strain. *Tectonophysics*, 636, 52-69. https://doi.org/10.1016/j.tecto.2014.08.011

Morniroli, J.P., Vankieken, D. & Winter, L. (1994). *Electron Diffraction. Dedicated Software to Kinematicaly Simulate CBED Patterns*. (USTL, Lille).

Morrison-Smith, D.J., Paterson, M.S., & Hobbs, B.E. (1976). An electron microscope study of plastic deformation in single crystals of synthetic quartz. *Tectonophysics*, 33, 43-79. https://doi.org/10.1016/0040-1951(76)90051-2

Mussi, A., Cordier, P., & Demouchy, S. (2015). Characterization of dislocation interactions in olivine using electron tomography. *Philosophical Magazine* 95, 335–345. https://doi.org/10.1080/14786435.2014.1000996.

Mussi, A., Cordier, P., Demouchy, S., & Hue, B. (2017). Hardening mechanisms in olivine single crystal deformed at 1090 °C: an electron tomography study. *Philosophical Magazine* 97, 3172–3185. https://doi.org/10.1080/14786435.2017.1367858

Mussi, A., Cordier, P., Ghosh, S., Garvik, N., Nzogang, B.C., Carrez, P., & Garruchet, S. (2016), Transmission electron microscopy of dislocations in cementite deformed at high pressure and high temperature. *Philosophical Magazine* 96, 1773–1789. https://doi.org/10.1080/14786435.2016.1177670

Mussi, A., Carrez, P., Gouriet, K., Hue, B., & Cordier, P. (2021a). 4D electron tomography of dislocations undergoing electron irradiation. *Comptes Rendus. Physique* 22-S3, 67-81. https://doi.org/10.5802/crphys.80

Mussi, A., Gallet, J., Castelnau, O., & Cordier, P. (2021b). Application of electron tomography of dislocations in beam-sensitive quartz to the determination of strain components. *Tectonophysics* 803, 228754. https://doi.org/10.1016/j.tecto.2021.228754

Nabarro, F.R.N. (1967). Steady-state diffusional creep. *Philosophical Magazine A* 16, 231-237. https://doi.org/10.1080/14786436708229736

Okudaira, T., Takeshita, T., Hara, I., & Ando, J.-I. (1995). A new estimate of the conditions for transition from basal <a> to prism [c] slip in naturally deformed quartz. *Tectonophysics* 250, 31-46. https://doi.org/10.1016/0040-1951(95)00039-4

Ord, A., & Christie, J.M. (1984). Flow stresses from microstructures in mylonitic quartzites of the Moine Thrust zone, Assynt area, Scotland. *Journal of Structural Geology*, 6, 639-654. https://doi.org/10.1016/0191-8141(84)90002-6

Pettersen, E.F., Goddard, T.D., Huang, C.C., Couch, G.S., Greenblatt, D.M., Meng, E.C., & Ferrin, T.E. (2004). UCSF Chimera: A visualization system for exploratory research and analysis. *J. Comput. Chem.* 25, 1605–1612. https://doi.org/10.1002/jcc.20084

Radon, J. (1983). Über die Bestimmung von Funktionen durch ihre Integralwerte längs gewisser Mannigfaltigkeiten. *Comput. Tomogr.* 69, 71–86. doi:10.1090/psapm/027/692055

Rutter, E.H., & Brodie, K.H. (2004). Experimental grain size-sensitive flow of hot-pressed Brazilian quartz aggregates. *Journal of Structural Geology* 26, 2011–2023. https://doi.org/10.1016/j.jsg.2004.04.006

Stipp, M., Stünitz, H., Heilbronner, R., & Schmid, S (2002a). The eastern Tonale fault zone: a natural laboratory for crystal plastic deformation of quartz over a temperature range from 250 to 700 C. *Journal of Structural Geology* 24, 1861-1884. https://doi.org/10.1016/S0191-8141(02)00035-4

Stipp, M., Stunitz, H., Heilbronner, R.& Schmid, S.M. (2002b). Dynamic recrystallization of quartz: Correlation between natural and experimental conditions. *Geol. Soc. London Spec. Publ.*, 200, 171–190. https://doi.org/10.1144/GSL.SP.2001.200.01.11

Stipp, M., Tullis, J., & Behrens, H. (2006). Effect of water on the dislocation creep microstructure and flow stress of quartz and implications for the recrystallized grain size piezometer. *Journal of Geophysical Research*, 111, 201-220. https://doi.org/10.1029/2005JB003852

Strachan, R.A., Smith, M., Harris, A.L., & Fettes, D.J. (2002). The Northern Highland and Grampian Terranes. In Trewin, N.H. (Ed.) The Geology of Scotland, 81-147, The Geological Society, London.

Sylvester, A.G. (1969). A microfabric study of calcite, dolomite, and quartz around Papoose Flat Pluton, California. *Geological Society of America Bulletin*. 80(7), 1311–1328. https://doi.org/10.1130/0016-7606(1969)80[1311:SMSOCD]2.0.CO;2

Taylor, G.I. (1938). Plastic strain in metals. *J. Inst. Met.* 62, 301–324.

Tokle, L., Hirth, G., & Behr, W.M. (2019). Flow laws and fabric transitions in wet quartzite. *Earth and Planetary Science Letters* 505, 152–161. https://doi.org/10.1016/j.epsl.2018.10.017

Trepied, L., & Doukhan, J.C. (1982). Evidence of ⟨a + c⟩ dislocations in synthetic quartz single crystals compressed along the c axis. *Bulletin de Minéralogie* 105 (2), 176–180. https://doi.org/10.3406/bulmi.1982.7601.

Tullis, J., Christie, J.M., & Griggs, D.T. (1973). Microstructures and preferred orientations of experimentally deformed quartzites, *Geol. Soc. Amer. Bull*, 84, 297-314.

Tullis, J., & Yund, R.A. (1989). Hydrolytic weakening of quartz aggregates: the effect of water and pressure on recovery. *Geophysical Research Letters* 16, 1343-1346. https://doi.org/10.1029/GL016i011p01343

Voisin T, Monchoux JP, Thomas M, Deshayes C, & Couret A. (2016). Mechanical Properties of the TiAl IRIS Alloy. *Metall. Mater. Trans. A*, 47, 6097–6108. https://doi.org/10.1007/s11661-016-3801-3

Vernooij, M.G.C. (2005). Dynamic recrystallisation and microfabric development in single crystals of quartz during experimental deformation. Ph.D. thesis, ETH Zürich, Nr. 16050, 128 pp. http://e-collection.ethbib.ethz.ch/show?type=diss&nr=16050

von Mises, R. (1928). Mechanik der plastischen Form¨anderung von Kristallen. *Z. für Angew. Math. Mech* 8, 161–185. https://doi.org/10.1002/zamm.19280080302.

Wallis, D., Parsons, A.J., & Hansen, L.N. (2019). Quantifying geometrically necessary dislocations in quartz using HR-EBSD: Application to chessboard subgrain boundaries. *Journal of Structural Geology* 125, 235-247. https://doi.org/10.1016/j.jsg.2017.12.012

Weathers, M.S., Bird, J.M., Cooper, R.F., & Kohlstedt, D.L. (1979), Differential stress determined from deformation-induced microstructures of the Moine thrust zone.

Journal of Geophysical Research, 84, 7495-7509. https://doi.org/10.1029/JB084iB13p07495

Weertman, J. (1968). Dislocation climb theory of steady-state creep. Transactions American Society Metals 61, 681–694.

Wenk, H.-R., Canova, G., Molinari, A., & Kocks, U.F. (1989). Viscoplastic modelling of texture development in quartzite, *Journal of Geophysical Research*, 94, 17895-17906. https://doi.org/10.1029/JB094iB12p17895

Wenk, H.-R., Yu, R., Vogel, S., & Vasin, R. (2019). Preferred orientation of quartz in metamorphic rocks from the Bergell Alps, *Minerals*, 9, 1-35. https://doi.org/10.3390/min9050277

White, S. (1977). Geological significance of recovery and recrystallization processes in quartz. *Tectonophysics*, 39, 143-170. https://doi.org/10.1016/0040-1951(77)90093-2

Yuan, S., Huang, M., Zhu, Y. & Li, Z. (2018). A dislocation climb/glide coupled crystal plasticity constitutive model and its finite element implementation. *Mech. Mater.*, 118, 44 – 61. https://doi.org/10.1016/j.mechmat.2017.12.009